

1 **Systematic benchmarking of imaging spatial transcriptomics platforms in FFPE tissues**

2 Huan Wang^{1,*}, Ruixu Huang^{2,*}, Jack Nelson^{1,*}, Ce Gao³, Miles Tran³, Anna Yeaton⁴, Kristen Felt⁵,

3 Kathleen L. Pfaff⁶, Teri Bowman⁷, Scott J. Rodig^{6,7}, Kevin Wei^{3,7}, Brittany A. Goods^{2,**}, Samouil

4 L. Farhi^{1,**}

5

6 **Affiliations**

7 ¹Spatial Technology Platform, Broad Institute of MIT and Harvard, Cambridge, MA 02142

8 USA.

9 ²Thayer School of Engineering, Molecular and Systems Biology, and Program in Quantitative
10 Biomedical Sciences at Dartmouth College, Hanover, NH 03755, USA.

11 ³Division of Rheumatology, Inflammation, and Immunity, Brigham and Women's Hospital and
12 Harvard Medical School, Boston, MA 02215, USA.

13 ⁴Present affiliation: Immunai, New York, NY 10016, USA.

14 ⁵ImmunoProfile, Brigham & Women's Hospital and Dana-Farber Cancer Institute, Boston, MA
15 02215, USA.

16 ⁶Center for Immuno-Oncology, Tissue Biomarker Laboratory, Dana-Farber Cancer Institute,
17 Boston, MA 02215, USA.

18 ⁷Department of Pathology, Brigham and Women's Hospital, Boston, MA 02215, USA.

19

20 * These authors contributed equally to this work

21 ** These authors jointly supervised this work

22

23 Corresponding author: Samouil L. Farhi: sfarhi@broadinstitute.org

24 Abstract

25 Emerging imaging spatial transcriptomics (iST) platforms and coupled analytical
26 methods can recover cell-to-cell interactions, groups of spatially covarying genes, and gene
27 signatures associated with pathological features, and are thus particularly well-suited for
28 applications in formalin fixed paraffin embedded (FFPE) tissues. Here, we benchmarked the
29 performance of three commercial iST platforms on serial sections from tissue microarrays
30 (TMAs) containing 23 tumor and normal tissue types for both relative technical and biological
31 performance. On matched genes, we found that 10x Xenium shows higher transcript counts per
32 gene without sacrificing specificity, but that all three platforms concord to orthogonal RNA-seq
33 datasets and can perform spatially resolved cell typing, albeit with different false discovery rates,
34 cell segmentation error frequencies, and with varying degrees of sub-clustering for downstream
35 biological analyses. Taken together, our analyses provide a comprehensive benchmark to guide
36 the choice of iST method as researchers design studies with precious samples in this rapidly
37 evolving field.

38 **MAIN**

39 Spatial transcriptomics (ST) tools measure the gene expression profiles of tissues or cells
40 *in situ*. These approaches overcome the limitations of single-cell RNA-sequencing (scRNA-seq)
41 methods by negating the need for cellularization and maintaining both local and global spatial
42 relationships between cells within a tissue. ST can thus recover cell-cell interactions with high
43 confidence, groups of spatially covarying genes, groups of cells predictive of cancer survival, and
44 gene signatures associated with pathological features ^[1, 2]. These advantages, coupled with rapidly
45 emerging computational and analytical methods, have led to substantial excitement about
46 deploying these platforms in fundamental biology studies, and in the clinic for research and
47 diagnostic purposes ^[3, 4, 5].

48 ST tools can be split into two broad categories: sequencing (sST) and imaging (iST) based
49 modalities. sST methods tag transcripts with an oligonucleotide address indicating spatial location,
50 most commonly by placing tissue slices on a barcoded substrate; isolating tagged mRNA for next-
51 generation sequencing; and computationally mapping transcript identities to locations ^[6]. In
52 contrast, iST methods most commonly use variations of fluorescence *in situ* hybridization (FISH)
53 where mRNA molecules are tagged with hybridization probes which are detected in a
54 combinatorial manner over multiple rounds of staining with fluorescent reporters, imaging, and
55 de-staining (**Fig. 1a**) ^[7]. Computational reconstruction then yields maps of transcript identity with
56 single-molecule resolution. Compared to sST methods, iST methods are targeted to subsets of the
57 transcriptome due to their reliance on pre-defined gene panels and they adopt the higher spatial
58 resolution and sensitivity of FISH, yielding single-cell resolution data ^[8].

59 While the iST methods share some similarities, significant differences arise in primary
60 signal detection and amplification, sample processing, and the subsequent fluorescent cycling

61 chemistry (**Fig. 1b**)^[9,10,11]. The need for amplification of signal is coupled to the sample processing,
62 namely whether the sample is cleared, gel-embedded, or photobleached to quench
63 autofluorescence. There are tradeoffs due to differences in sample processing for each iST method.
64 For example, clearing of the sample increases signal quality but can prevent follow-up H&E
65 staining and complicate immunostaining, which, in turn, can make cell segmentation more
66 challenging. Finally, there are tradeoffs between imaging time, molecular plex, and imaging area
67 covered, which result from the particular combination of the molecular protocol and the imaging
68 hardware implementation^[12].

69 A key historic limitation in the widespread use of iST methods with human clinical samples
70 was the incompatibility of most methods with formalin-fixed, paraffin-embedded (FFPE) tissue
71 samples^[13, 14]. FFPE is the standard format for clinical sample preservation for pathology due to
72 its ability to maintain tissue morphology and sample stability at room temperature for decades^[15].
73 The ability to process FFPE samples with iST would enable the use of archival tissue banks for
74 studies and obviate the need for specialized sample harvesting workflows. However, FFPE
75 samples tend to suffer from decreased RNA integrity, particularly after having been stored in
76 archives for extended periods of time^[16].

77 Three companies recently released the first FFPE compatible commercial iST platforms:
78 10x's Xenium, NanoString's CosMx, and Vizgen's MERSCOPE^[9,10,11,17]. These three platforms
79 each use different protocols, probe designs, signal amplification strategies, and computational
80 processing methods, and therefore may potentially yield different sensitivities and downstream
81 results. The main chemistry difference lies in transcript amplification: 10x Xenium uses a small
82 number of padlock probes with rolling circle amplification; CosMx uses a low number of probes
83 amplified with branch chain hybridization; and MERSCOPE uses direct probe hybridization but

84 amplifies by tiling the transcript with many probes (**Fig. 1b**). However, no head-to-head
85 performance comparisons on matched samples have been published. Understanding the key
86 differences across platforms will allow users to make better-informed decisions regarding panel
87 design, method choice, and sample selection as they design costly experiments, often on precious
88 samples that have been bio-banked for years [18].

89 In this study, we compared currently available FFPE-compatible iST platforms on matched
90 tissue samples. We prepared a set of samples representative of typical archival FFPE tissues,
91 comprised of 23 different tissue types, and acquired matched data from sequential sections
92 according to the manufacturer's best practices at the time of writing, generating a dataset of > 3.3M
93 cells. We analyzed the relative sensitivity and specificity of each method on shared transcripts,
94 and further quantified the concordance of the iST data across each platform with orthogonal data
95 sets from The Cancer Genome Atlas (TCGA) program and Genotype-Tissue Expression (GTEx)
96 databases [19,20]. Then we focused on cell-level comparisons, evaluating the out-of-the-box
97 segmentation for each platform based on detected genes and transcripts and coexpression patterns
98 of known disjoint markers. Finally, we cross-compared the ability of each platform to identify cell
99 type clusters with breast and breast cancer tissues as an example use case. Taken together, our
100 work provides the first head-to-head comparison of these platforms across multiple archival
101 healthy and cancerous FFPE tissue types.

102 **RESULTS**

103 **Collection of matched iST data across 23 FFPE tissue types reveals high transcript counts**
104 **obtained by Xenium and CosMx.**

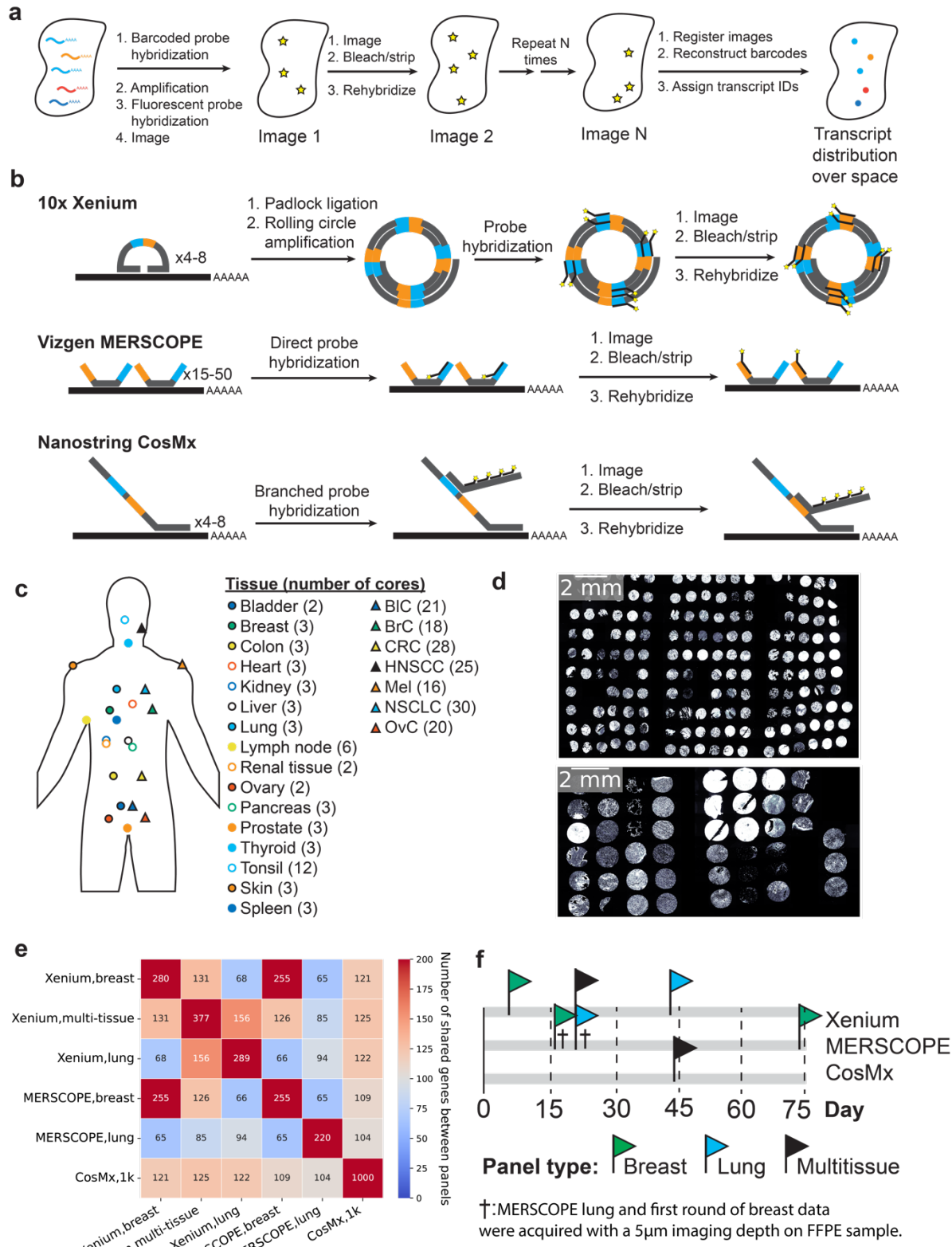
105 To test the performance of the latest generation of FFPE-compatible iST tools, we
106 measured the spatial expression of the same genes on the same samples as much as possible given
107 current panel configurations. To accomplish this, we used two previously generated multi-tissue
108 tissue microarrays (TMAs) from clinical discarded tissue (**see Methods**). We focused on FFPE
109 tissues as the standard method for sample processing and archival in pathology. One TMA
110 consisted of one hundred and seventy 0.6 mm diameter cores (i.e. sampled regions) from seven
111 different cancer types, with 3-6 patients per cancer type, and 3-6 cores per patient (**Fig. 1c-d, Supple-**
112 **mentary Table 1**). A separate TMA consisted of forty-five 1.2 mm diameter cores
113 spanning sixteen normal tissue types isolated with each tissue type coming from one patient and
114 represented in 2-3 cores (**Fig. 1c-d, Supplementary Table 2**). CosMx and Xenium suggest pre-
115 screening samples based on H&E, while MERSCOPE recommends a DV₂₀₀ > 60%. Since our goal
116 was to determine the compatibility of iST platforms under typical workflows for biobanked FFPE
117 tissues, and since TMAs are challenging to assay by DV₂₀₀, samples were not prescreened based
118 on RNA integrity. Samples were screened by H&E in the process of TMA assembly. Both TMAs
119 were sliced into serial sections for processing by 10x Xenium, Vizgen MERSCOPE, and
120 NanoString CosMx, following manufacturer instructions (**see Methods**).

121 The three different iST platforms offer different degrees of customizability and panel
122 compositions. In terms of panel design, MERSCOPE and Xenium offer either fully customizable
123 panels or standard panels with optional add-on genes, while CosMx offers a standard 1K
124 (substantially larger plex) panel with optional add-on genes. We opted to run the CosMx 1K panel

125 as available commercially, as well as the Xenium human breast, lung, and multi-tissue off-the-
126 shelf panels. We then designed two MERSCOPE panels to match the pre-made Xenium breast and
127 lung panels, by filtering out any genes which could potentially lead to high expression flags in any
128 tissue in the Vizgen online portal. This resulted in a total of six panels, with each panel overlapping
129 the others on > 94 genes (**Fig. 1e, Supplementary Table 3**). Samples were run following
130 manufacturer instructions over the course of 74 days after slicing (**Fig. 1f, Supplementary Table**
131 **4**), with efforts made to ensure that head-to-head comparisons were available at similar time points
132 for each pair of platforms. In data review, we noticed that MERSCOPE breast and lung panel were
133 originally acquired with a 5 μm imaging depth, which was unintentionally thinner than the
134 manufacturer recommendation of 10 μm , and could thus lead to aberrantly low counts. Thus, a
135 second round of breast panel acquisition was performed with a 10 μm imaging depth
136 (**Supplementary Table 1a**), resulting in a median 3.0-fold increase in expression across all
137 transcripts. We excluded the 5 μm MERSCOPE breast panel data from all further comparisons but
138 left the lung panel data in as an illustrative example of an unsuccessful run. However, we
139 emphasize that MERSCOPE performance should be judged based on the rerun breast panel.

140 Each data set was processed according to the standard base-calling and segmentation
141 pipeline provided by each manufacturer. The resulting count matrices and detected transcripts were
142 then subsampled and aggregated to individual cores of the TMA (**Methods**). Across all datasets
143 we generated >190 million transcripts, >3.3 million cells, across 7 tumor types, and 16 normal
144 tissue types. Overall, we found that the cores from each TMA were generally well adhered to the
145 tissue and detected transcripts, and we were able to collect data from all three modalities for 217
146 cores (**Supplementary Table 4**). The total number of transcripts recovered for each run was
147 highest for Xenium, followed closely by CosMx, and then MERSCOPE (**Supplementary Table**

148 4). The total number of cells initially reported was highest for Xenium followed by MERSCOPE
149 and CosMx (**Supplementary Table 4**). Based on the initially reported number of transcripts, the
150 tumor TMA appeared to provide more counts than the normal tissue TMA, which we ascribed to
151 a higher tissue quality in the tumor samples (**Supplementary Table 4**). We note that the total
152 number of transcripts from the MERSCOPE normal TMA run was below what would be typically
153 thought of as a successful run, even when rerunning with the breast panel at 10 μm imaging depth.
154 Such a sample would normally be excluded from analysis, but we continued the data through to
155 illustrate how low transcript capture affects downstream results.



156

157 **Figure 1: Experimental design and iST platforms.** (a) Overall approach for generating iST data.

158 (b) Different amplification approaches for Xenium, MERSCOPE, and CosMx. (c) Overview of

159 the tissue types and numbers of cores used in this study. BlC = bladder cancer, BrC = breast cancer,
160 CRC = colorectal cancer, HNSCC = head and neck squamous cell carcinoma, Mel = Melanoma,
161 NSCLC = non-small cell lung cancer, OvC = ovarian cancer. (d) DAPI images from the Xenium
162 run of each TMA, including tumors (top) and normal tissues (bottom) (e) The number of common
163 target genes in each panel used in this study. (f) Overall timeline of the imaging days for each
164 study. Day = 0 corresponds to the day of slicing. † denotes the MERSCOPE breast and lung panels
165 acquired with a 5 μ m imaging thickness, thinner than manufacturer instructions.
166

167 **10x Xenium shows higher transcript counts per gene without sacrificing specificity**

168 We next sought to directly compare the performance of each iST platform on matched
169 genes. We began with a pseudo-bulk-based approach at the core level since this would not depend
170 on differences in cell segmentation performance (see **Methods**)^[21].

171 First, we examined the run-to-run reproducibility within a single platform for Xenium and
172 MERSCOPE, finding that the total transcript count of all shared genes was highly correlated across
173 data sets acquired with different panels, regardless of the tissue of origin (**Supplementary Fig.**
174 **1a**). We also examined the pseudo-bulk gene expression correlation for cores from the same patient
175 in the same dataset and found that correlation was high (Pearson's $r \Rightarrow 0.7$) in almost all cases
176 (**Supplementary Fig. 1b-c**), indicating good sample-to-sample reproducibility within a given
177 platform.

178 To evaluate the relative sensitivity of each platform, we plotted the total transcript counts
179 of every shared gene between all combinations of platform and panel, summed across all matched
180 cores. We found generally linear relationships between all pairs of platforms (**Fig. 2a-c**,
181 **Supplementary Fig. 2**). Xenium consistently showed higher expression levels on the same genes
182 than CosMx in the tumor TMA, with the Xenium breast having 14.6-fold more counts than the
183 CosMx multi-tissue data sets (**Fig. 2a**). The Xenium multi-tissue panel data showed a slightly
184 smaller difference, with 12.3-fold higher expression on the same genes (**Fig. 2a**), while the lung

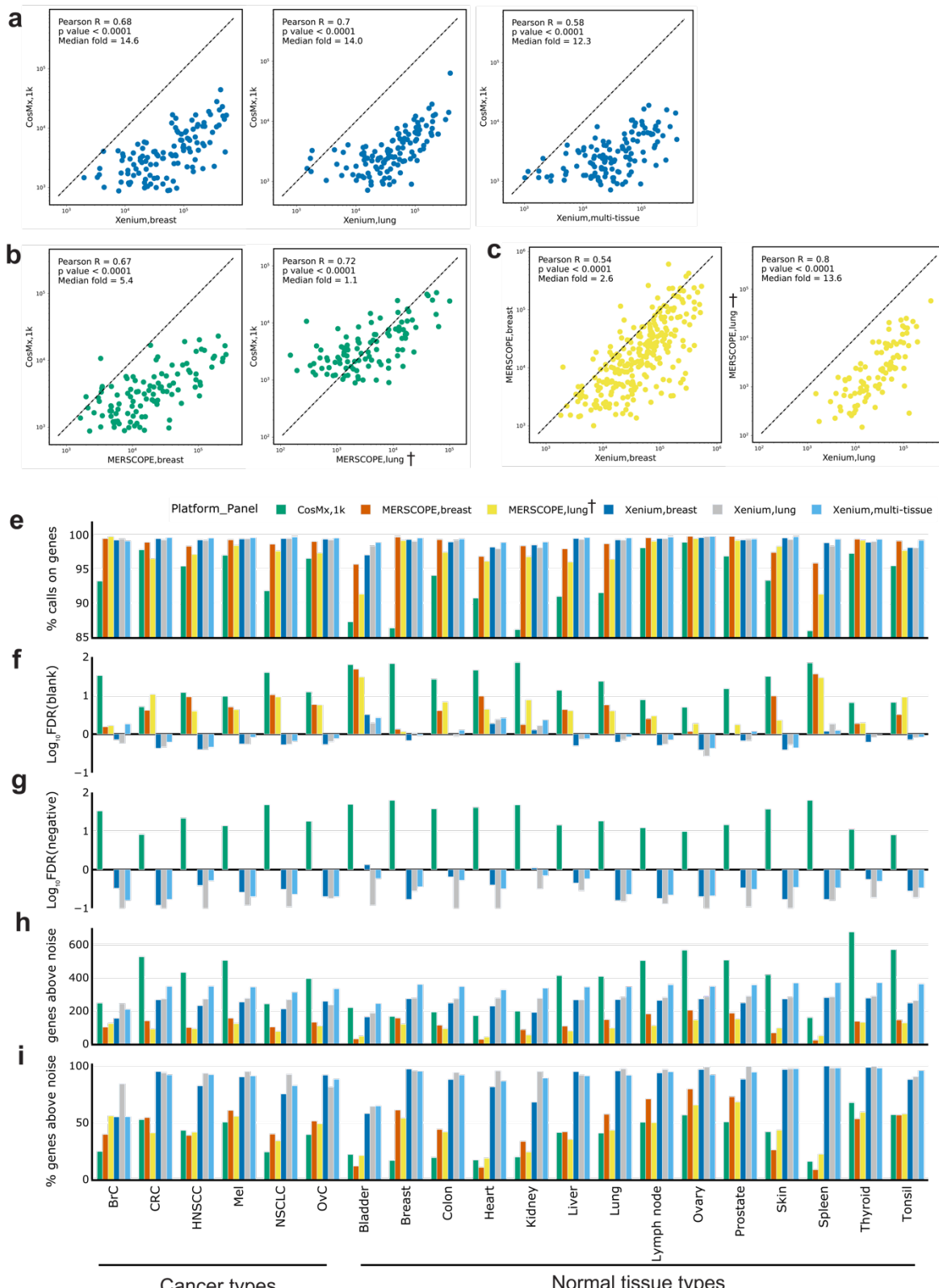
185 panel, which was acquired closest in time following slicing, also displayed a median of 14.0-fold
186 higher expression (**Fig. 2a**). MERSCOPE showed higher expression levels than CosMx when
187 using the breast (10 μm) panel (median of 5.4-fold higher), and comparable expression levels even
188 when using the lung (5 μm) panel (median of 1.1-fold) (**Fig. 2b**). Finally, Xenium showed 2.6-
189 fold higher median expression with the breast panels (10 μm) than MERSCOPE, and 13.6-fold
190 higher median expression with the lung panels (5 μm) (**Fig. 2c**). In the normal tissue TMA, we
191 found that results were generally consistent, except that the MERSCOPE breast panel showed
192 decreased transcript counts relative to the same panel in the tumor TMA (**Supplementary Fig. 2b-**
193 **c**), which is consistent with this TMA being unsuccessful for MERSCOPE. Considering the overall
194 higher transcripts per cell across platforms for the tumor TMA (**Supplementary Table 4**), this
195 suggests that the ability to detect transcripts falls off more strongly with sample quality with
196 MERSCOPE, altering the performance relative to CosMx but not Xenium. Examining the CosMx
197 as compared to Xenium data also revealed an upward curve in the lower expression regime
198 indicative of higher-than-expected calls associated with the low expression regime by CosMx
199 (**Supplementary Fig. 2a**).

200 We next wanted to assess the specificity of each platform. Each of the three platforms
201 includes negative controls which are used to evaluate sample quality [22, 23]. Xenium and CosMx
202 include both negative probes (e.g. real probes targeting nucleic acids that are not present in human
203 tissue) and negative barcodes (e.g. algorithmically allowable barcodes that are not associated with
204 any probe in the experimental panel). MERSCOPE includes only negative barcodes by default. To
205 determine specificity, we first calculated the fraction of negative barcodes and probes relative to
206 the number of transcripts for each tissue type (**Fig. 2e**). We found that MERSCOPE and Xenium
207 consistently showed the highest on-target fraction, while CosMx was lower across each tissue type

208 (Fig. 2e). However, this measurement is biased because of the relative numbers of controls and
209 target barcodes. We therefore also adopted a false discovery rate (FDR) calculation which
210 normalizes for these differences and is calculated against both the negative probes and negative
211 barcodes (see **Methods**, Fig. 2f-g). We found that Xenium consistently showed the lowest FDR
212 while CosMx showed the highest FDR regardless of whether we standardized to negative control
213 barcodes or probes. This finding is consistent with the upswing in the gene-gene expression plots
214 in **Fig 2a** and **Supplementary Fig. 2a**—as both indicate a higher FDR at the low end of the gene
215 expression range. These results are consistent when visualized across panels (**Fig. 2e-g**).

216 Finally, we used the negative control barcodes to evaluate the number of genes reliably
217 detected by each platform in each tissue type. For each core, we calculated the number of genes
218 that were detected two standard deviations above the average expression of the negative control
219 probes. These numbers were then averaged for cores of the same tissue type. Because the CosMx
220 panel was almost three times larger, it yielded a larger absolute number of detected genes in 14
221 out of 20 tissue types while the Xenium breast panel was higher in the remaining 6 tissue types
222 (**Fig. 2h, Supplementary Table 5**). However, Xenium consistently detected the highest fraction

223 of genes in a panel, followed by MERSCOPE and CosMx (Fig. 2i).



225 **Figure 2: Technical performance comparison of iST platforms grouped by tissue types. (a)**
226 Scatter plots of summed gene expression levels (on a logarithmic scale) of every shared gene
227 between Xenium (breast/lung) and CosMx (1k) data, captured from matched tumor TMA cores.
228 Each data point corresponds to a gene. **(b)** Same as (a) but between MERSCOPE (breast/lung) and
229 CosMx(1k). **(c)** Same as (a) but between Xenium(breast/lung) and MERSCOPE(breast/lung). **(d)**
230 Same as (a) but between Xenium(multi-tissue) and CosMx(1k). **(e)** Bar plot of percentage of all
231 transcripts corresponding to genes relative to the total number of calls (including negative control
232 probes and unused barcodes) averaged across cores of the same tissue type. Results are presented
233 by panel including breast, lung, and multi-tissue panels from Xenium; breast and lung panels from
234 MERSCOPE; and multi-tissue 1k panel from CosMx. **(f)** Bar plot of false discovery rate
235 (FDR) where $FDR(\%) = (\text{blank barcode calls} / \text{total transcript calls}) \times (\text{Number of panel genes} / \text{Number of blank barcode}) \times 100$. FDR values were \log_{10} transformed to better show the
236 differences between panels. **(g)** Same as (f) but using negative control probes to replace blank
237 barcodes. MERSCOPE is missing in this bar plot as it does not have negative control probes by
238 design. **(h)** Bar plot of number of genes detected above noise, estimated as two standard deviations
239 above average of the negative control probes. **(i)** Same as (h) but normalized to the number of
240 genes in a panel. † denotes the MERSCOPE lung panel acquired with a 5 μm imaging thickness.
241
242

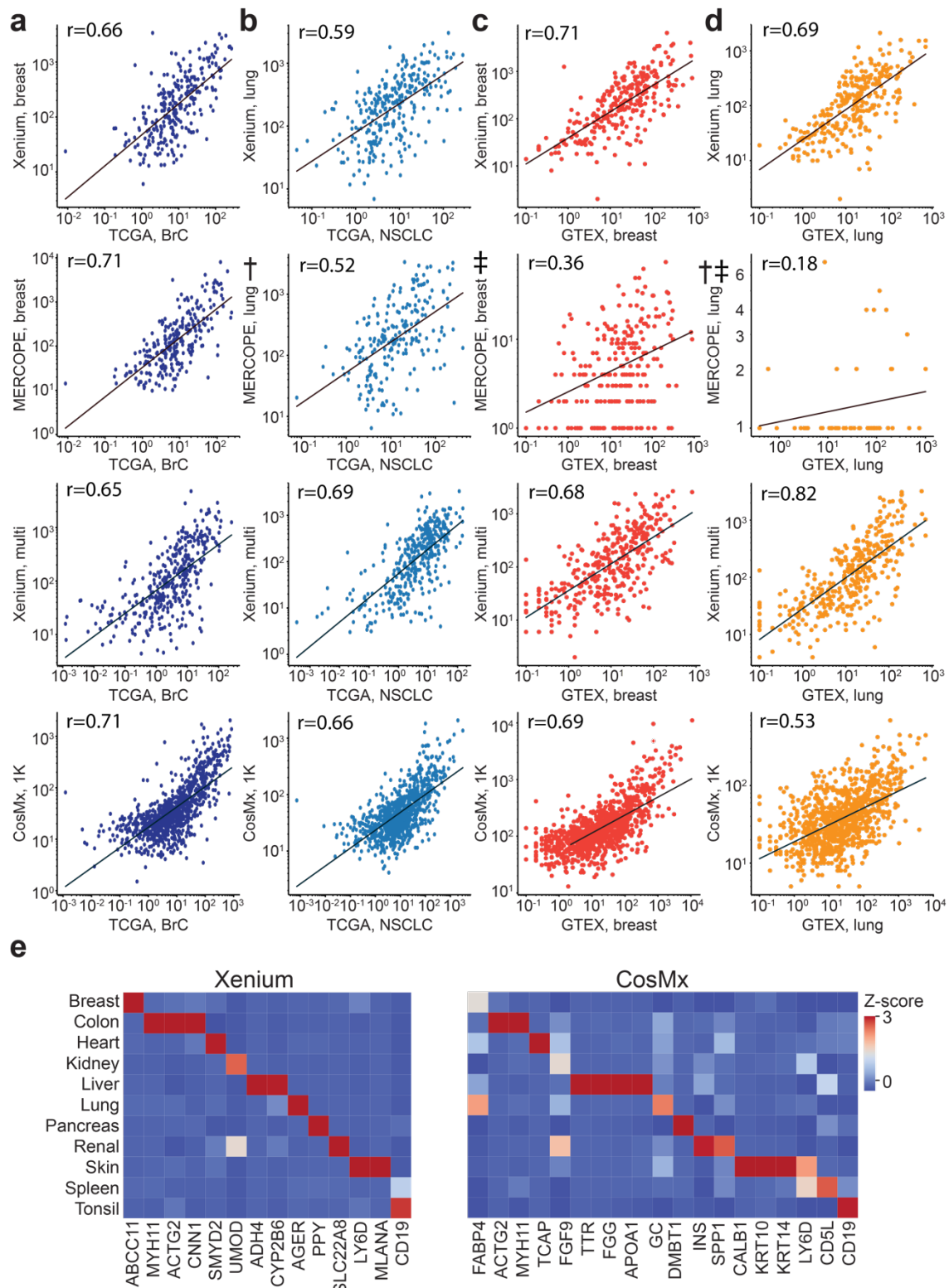
243 **iST platforms are all concordant with orthogonal RNA-seq data sets**

244 In the absence of ground truth, it is difficult to evaluate whether a higher number of
245 expressed genes is representative of increased sensitivity to real biology or increased false positive
246 rates. We thus evaluated the correlation of iST data to reference RNA-seq data. We first aggregated
247 pseudo-bulk normal tissue TMA results from all panels of the three platforms and compared them
248 to data from the TCGA program (see **Methods**)^[11]. We observed similar correlation coefficients
249 across all gene panels relative to pseudo-bulk RNA-seq expression data (**Fig. 3a-b**,
250 **Supplementary Table 8**). However, notably, the CosMx data showed a characteristic upswing in
251 the low expression regime, similar to that observed when plotting gene-by-gene expression against
252 MERSCOPE and Xenium (**Fig. 2, Supplementary Fig. 2**).

253 We also compared the pseudo-bulk results from the normal tissue TMA with bulk RNA-
254 seq data obtained from GTEx^[12]. The Xenium breast, Xenium multi-tissue, and CosMx data sets
255 showed similar correlations to breast data obtained from GTEx, while the MERSCOPE had

256 significantly lower correlation, consistent with a run which doesn't pass QC (Pearson's r of 0.36
257 vs 0.71, 0.68, and 0.69, respectively, **Fig. 3c**). Similar trends were observed in the lung data, with
258 MERSCOPE lung (5 μ m) showing the lowest correlation while the other three data sets showed
259 higher correlations to GTEx data (**Fig. 3d**). These relative trends remained true across most normal
260 tissue types, though we found that thyroid, pancreas, and lymph nodes showed the lowest
261 correlations across all panels while prostate, tonsil, and liver showed the highest correlations
262 (**Supplementary Table 9**). Overall, our comparison to TCGA and GTEx data suggests that while
263 some platforms may be more highly correlated to reference datasets in some cases, all are within
264 a similar correlation regime regardless of tissue type.

265 We next wanted to determine how the expression of tissue-specific transcript markers
266 varied across each platform. To accomplish this, we curated tissue markers that are unique to each
267 tissue type by selecting genes whose expression in a single tissue exceeds 20 times the sum of
268 other tissues from the GTEx database (see **Methods**). We found tissue-specific expression patterns
269 of several of these markers across all selected panels when visualized across each healthy tissue
270 type (**Fig. 3e**). MERSCOPE showed expression of tissue-specific markers in multiple tissue types,
271 yet some canonical markers were not enriched in certain tissues, potentially caused by the
272 unsuccessful normal TMA data acquisition (Supplementary Fig. 3b). Although CosMx showed
273 satisfying expression patterns for some tissue markers, many canonical markers are not enriched
274 in the expected tissues, possibly due to the high false discovery rate (**Fig. 3f-g**). Across marker
275 genes, Xenium data had a distinct expression pattern in all tissues, whereas CosMx and
276 MERSCOPE showed a less distinct pattern in many tissue types.



277

278 **Figure 3: Concordance of iST data with reference RNA-seq datasets.** (a) Scatter plots of
 279 overlapping genes, showing the averaged expression of a gene across breast cancer cores profiled
 280 by the indicated panel, normalized to 100,000 vs the average FPKM from TCGA for all samples

281 of a matched tissue type (BRCA). **(b)** Same as (a) but for lung cancer cores plotted vs averaged
282 LUAD and LUSC samples from TCGA. **(c)** Same as (a) but showing breast cores vs averaged
283 nTPM values from GTEx breast samples. **(d)** Same as (a) but for lung cores and samples. † denotes
284 the MERSCOPE lung data acquired with a 5- μm imaging depth on FFPE sample. ‡ denotes the
285 normal tissue TMA data of MERSCOPE which failed initial QC. **(e)** Heatmap of Z-scored average
286 gene expression for several canonical marker genes in the indicated tissue cores for the Xenium
287 multi-tissue panel (left) and CosMx 1K panel (right).

288

289 **Out of the box segmentation and filtration can yield cells with comparable numbers of**
290 **detected transcripts and genes from each platform.**

291 Next, we compared the performance of each iST method on a single-cell level. The three
292 platforms generate cell boundaries based on a DAPI image alone (Xenium) or a DAPI image
293 combined with a membrane marker (CosMx and MERSCOPE). When we visually examined the
294 segmentation outputs, Xenium data showed cell boundaries that appeared to include large regions
295 of non-cellular space, in contrast to MERSCOPE and CosMx which tightly followed the visualized
296 cell nucleus (**Fig. 4a**). When transcripts were overlaid with these segmentation boundaries,
297 Xenium cell boundaries fell between regions of transcripts and thus most transcripts were assigned
298 to cells. MERSCOPE and CosMx's tighter nuclei removed more transcripts, though those that
299 remain appeared more confidently assigned to cells. Overall, when normalized to the imaged tissue
300 area, Xenium and CosMx identified the most putative cells, followed by MERSCOPE (**Fig. 4b**,
301 **Supplementary Table 6**). In line with the visual inspection, Xenium cells were consistently larger,
302 regardless of data set or panel, followed by CosMx and finally MERSCOPE (**Fig. 4c**,
303 **Supplementary Table 7**).

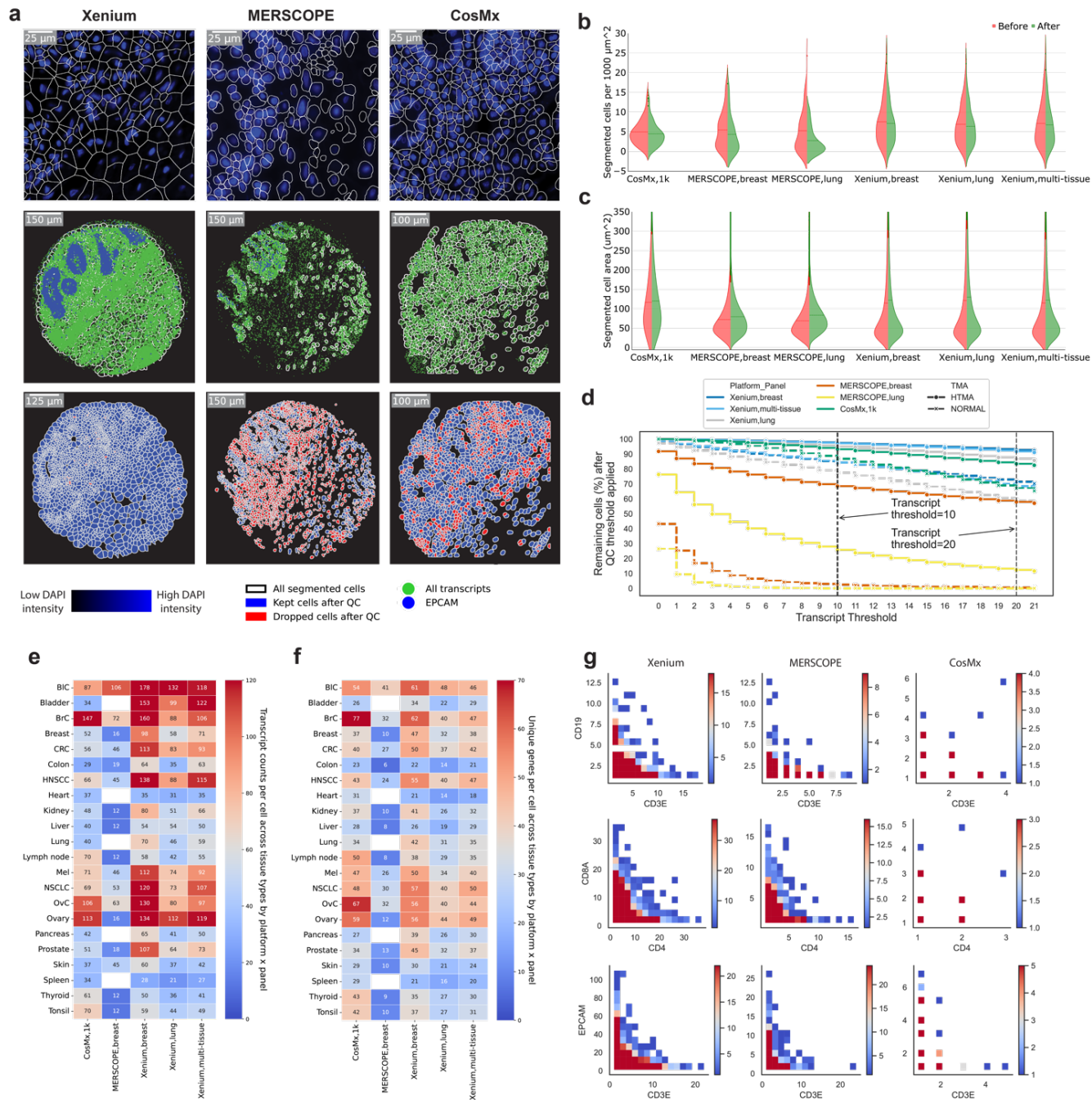
304 We filtered out empty regions of space and cells without any transcripts for downstream
305 examination and quantified the fraction of cells containing differing numbers of transcripts per cell
306 (**Fig. 4d**). We chose a permissive threshold of removing cells with fewer than 10 transcripts for
307 Xenium and MERSCOPE, and 20 transcripts for CosMx from downstream analysis. [11, 24, 25]. The

308 tumor TMA consistently had a greater fraction of cells passing filtration, with Xenium retaining
309 the most cells (97.43% breast, 97.10% multi-tissue, 95.08% lung) followed by CosMx (83.41%)
310 and MERSCOPE (68.46% breast (10 μm), 25.77% lung (5 μm) (**Supplementary Table 3**). The
311 normal tissue TMA had overall lower cell retention performance, but the relative performance of
312 the platforms based on the fractions of cells remained the same. Notably, while CosMx and
313 Xenium still retained > 77% of the cells, MERSCOPE data of the normal tissue TMA had < 3%
314 of cells retained and was thus not used in downstream analysis. Unsurprisingly, filtration decreased
315 the number of retained cells per unit area for all platforms, with the smallest decrease coming for
316 CosMx. The cells retained from CosMx had similar areas, while filtration of the Xenium and
317 MERSCOPE data sets resulted in a higher average cell area (**Fig. 4c**).

318 After filtration, we compared the number of transcripts and the number of unique genes
319 per retained cell across all tissues and all panels, focusing only on cores that were sampled by all
320 three platforms (**Fig. 4e-f**). Xenium breast panel gave the highest numbers of transcripts per cell
321 in most tissue types, 17 out of 22. The CosMx data showed the highest numbers of transcripts in
322 heart, lymph node, spleen, thyroid, and tonsil; and comparable transcript counts in breast cancer,
323 ovary, and ovarian cancer to the Xenium breast panel. The MERSCOPE data generally had the
324 lowest number of transcripts per cell, though bladder cancer and breast cancer measured with the
325 MERSCOPE breast panels approached the results from Xenium, and the bladder cancer and skin
326 data sets had higher transcripts per cell than CosMx. As expected given its larger panel size,
327 CosMx found many unique genes per cell, showing the largest numbers in 9 tissue types: breast
328 cancer, colon, heart, lymph node, ovary, ovarian cancer, spleen, thyroid, and tonsil; while Xenium
329 breast panel found the most unique genes per cell in 12 tissue types: bladder cancer, bladder, breast,
330 CRC, HNSCC, kidney, lung, melanoma, NSCLC, pancreas, prostate, and skin (**Fig. 4f**). If these

331 analyses were restricted to only the shared genes across all panels, numbers were much lower, but
332 Xenium showed higher expression levels and unique numbers of genes than either CosMx or
333 MERSCOPE (**Supplementary Fig 3c-d**).

334 We then wanted to determine how effectively different iST platforms' segmentation
335 algorithms perform. We examined the co-expression of *CD19*, a canonical B-cell marker, and
336 *CD3e*, a canonical T-cell marker across all filtered cells; the co-expression of *CD8* and *CD4*,
337 markers of T-cell subsets; and the co-expression of *CD3e* and *EPCAM*, a marker for epithelial
338 cancer cells [26, 27]. All these marker gene pairs are disjointly expressed, and a well-performing
339 segmentation algorithm should yield few cells expressing both markers. We pooled all the filtered
340 cells from matched cores and all available panels of each platform and plotted the expression of
341 one gene against the other and converted the scatter plot to a heatmap to show cell fractions. We
342 found that Xenium—despite its less visually accurate cell boundaries—and MERSCOPE, showed
343 clear patterns of disjoint expression, separating cells from different lineages, while CosMx showed
344 such a pattern for *EPCAM* vs *CD3e* but not for the other two pairs (**Fig. 4g**). Given the low counts
345 of the immune genes, it was difficult to determine if these were false positive calls or segmentation
346 errors. Nevertheless, since the CosMx panel is much higher plex, and retained similar numbers of
347 transcripts and genes to Xenium, we wondered how these two methods performed in terms of cell
348 type recovery.



349

350 **Figure 4: Comparison of cell segmentation results from each iST platform. (a)** Top row: DAPI
351 image overlaid with cell segmentation boundaries (subset). Middle row: all the transcripts in green
352 dots, white lines for the cell boundaries, and *EPCAM* in blue dots. Bottom row: segmented cell
353 boundaries before and after filtration. **(b)** Violin plot of segmented cells per unit area before (left
354 half) and after filtration (right half) grouped by panel with tumor and normal TMA data combined.
355 **(c)** Same as (b) but showing cell areas before and after filtration. **(d)** Line plot showing remaining
356 cells in percentage after filtering with various thresholds (transcripts per cell). Dotted lines indicate
357 selected thresholds: 10 transcripts or above for Xenium and MERSCOPE and 20 for CosMx. **(e)**
358 Heatmap of transcripts per cell after filtration. All available genes are considered here for each

359 panel. MERSCOPE lung panel (5 μm) was excluded from this heatmap. **(f)** Same as **(e)** but
360 showing unique genes per cell. **(g)** Co-expression density map for three pairs of disjoint genes
361 (rows) from all three platforms (columns). All cells across all tissues which include at least one
362 detected transcript of either of the indicated genes are plotted together, with color indicating the
363 number of cells at the indicated expression levels of each gene.
364

365

366 Clustering analyses reveal differences in cell type recovery across platforms

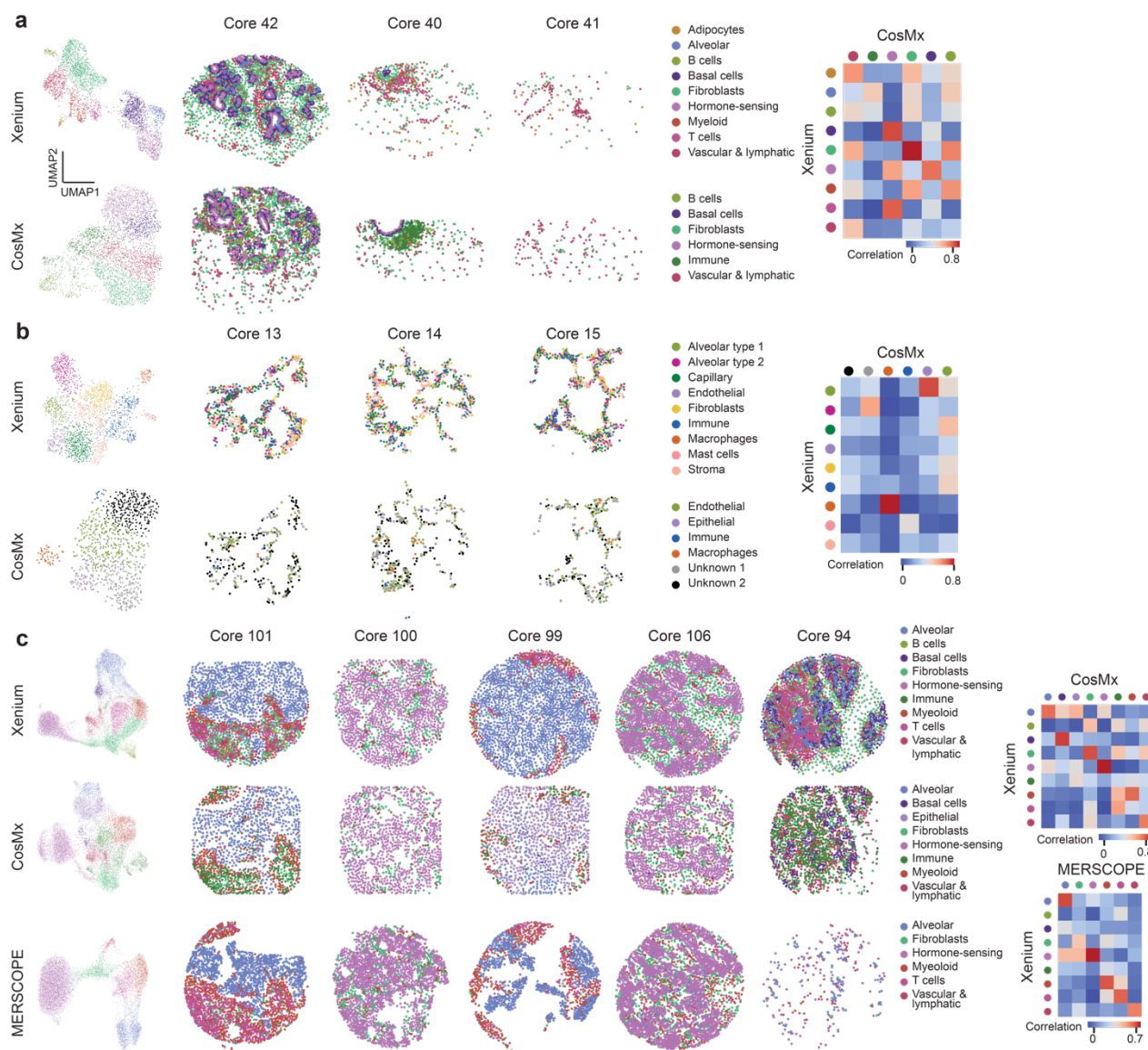
367 In a typical iST workflow, a key step is reducing the dimensionality of the data by
368 identifying cell types, their unique states, and their expression patterns for further analysis
369 leveraging spatial information^[28]. To compare across platforms, we clustered the data from the
370 filtered cells from all the cores for each TMA with a focus on breast tissues. The initial clustering
371 of TMAs from datasets (except MERSCOPE normal tissue) showed expected batch effects caused
372 by patients and tissue types with broadly similar cluster arrangements around morphological tissue
373 features (**Supplementary Fig. 4a-d**). We removed batch effects (see **Methods**) and then
374 performed targeted clustering and cell type annotation for breast samples from the CosMx and
375 Xenium breast datasets; lung samples from the CosMx and Xenium lung datasets; and breast
376 cancer from the CosMx, MERSCOPE breast, and Xenium breast datasets.

377 In breast samples, we were able to identify nine cell types, including all known major cell
378 types, (adipocytes, alveolar cells, B cells, basal cells, fibroblast cells, hormone-sensing cells,
379 myeloid, T cells, vascular & lymphatic cells) from the Xenium data, using previously established
380 markers (**Fig. 5a, Supplementary Fig. 5**)^[29,30,31]. In the CosMx data, we were only able to identify
381 six cell types, including several major cell types, but failed to recognize cell subtypes (B cells,
382 basal cells, fibroblast, hormone-sensing cells, immune cells, and vascular & lymphatic cells) (**Fig.**
383 **5a, Supplementary Fig. 5**). A high gene-to-gene correlation was found between all overlapping
384 cell types between Xenium and CosMx (**Fig. 5a**). Similarly, in the lung samples, we were able to

385 identify nine cell types (alveolar epithelial type 1 cell, alveolar epithelial type 2 cell, endothelial
386 capillary cells, endothelial cells, fibroblasts, immune cells, macrophages, mast cells, and stroma
387 cells) in the Xenium lung panel, successfully covering all known major cell types (**Fig. 5b**,
388 **Supplementary Fig. 5**) [32,33]. Four of the six major clusters were identified and annotated in the
389 lung samples from the CosMx data (endothelial cells, epithelial cells, immune cells, and
390 macrophages), while the other two clusters remained difficult to annotate due to the non-traditional
391 enriched gene markers (**Fig. 5b, Supplementary Fig. 5**). Correlation heatmaps show a strong
392 correlation between the two macrophage clusters identified in Xenium and CosMx (**Fig. 5b**). The
393 epithelial cell cluster from CosMx correlates strongly with alveolar epithelial type 1 cell from
394 Xenium and the endothelial cell cluster from CosMx correlates with endothelial capillary cell
395 cluster from Xenium (**Fig. 5b**).

396 Finally, in breast cancer, after batch effect removal (**Supplementary Fig. 5d-f**), Xenium
397 resulted in nine cell types (alveolar cells, B cells, basal cells, fibroblast, hormone-sensing cells,
398 immune cells, myeloid, T cells, and vascular & lymphatic cells) (**Fig. 5c, Supplementary Fig. 5**)
399 [34,35,36]. On the other hand, CosMx resulted in eight cell types (alveolar cells, basal cells, epithelial
400 cells, fibroblast cells, hormone-sensing cells, immune cells, myeloid, and vascular & lymphatic
401 cells). MERSCOPE resulted in six cell types, including alveolar cells, fibroblast cells, hormone-
402 sensing cells, myeloid cells, T cells, and vascular & lymphatic cells. The cell type annotation of
403 Xenium and CosMx is comparable in terms of both transcriptomic profile and subtype depth, with
404 CosMx only unable to annotate immune cell subtypes (B cell and T cell). Gene expression of the
405 same cell type from both platforms correlated well (**Fig. 5c, Supplementary 5**). The cell type
406 annotation of CosMx, however, was especially difficult compared to Xenium because of its
407 atypical gene markers shown for each cluster in the heatmaps (**Supplementary Fig. 5**) and low

408 expression of transcripts from canonical markers (**Supplementary Fig. 5g-h**). MERSCOPE, on
409 the other hand, identified most, but not all, the cell types recognized by Xenium and CosMx,
410 including alveolar cells, fibroblast cells, hormone-sensing cells, myeloid, T cells, and vascular &
411 lymphatic cells. MERSCOPE and Xenium showed a high correlation for almost all matching
412 clusters. The correlation map shows a clearer one-to-one mapping between MERSCOPE and
413 Xenium clusters than Xenium and CosMx clusters.



414
415

416 **Figure 5: Cell type recovery performance across technology. (a)** Clustering results of breast
417 samples in normal TMA from Xenium breast panel and CosMx multi-tissue panel. Correlation
418 plot showing the correlation between cell types identified. **(b)** Clustering results of lung samples
419 in normal TMA from Xenium lung panel and CosMx multi-tissue panel. Correlation plot showing
420 the correlation between cell types identified. **(c)** Clustering results of breast cancer samples in
421 tumor TMA from Xenium breast panel, MERFISH breast panel, and CosMx multi-tissue panel.
422 Correlation plot showing the correlation between cell types identified in CosMx and Xenium as
423 well as MERFISH and Xenium.
424

425 **DISCUSSION**

426 In this study, we compared data obtained with three commercially available iST platforms
427 with archival FFPE tissues to assess overall technical performance and help guide experimental
428 design with human samples that represent an important use case of these platforms. We focused
429 our analyses on technical performance as a function of tissue type, including 7 different tumor
430 types and 16 normal tissue types. Overall, we found that each iST platform presented various
431 tradeoffs in terms of implementation, panel design and panel options, and resulting total transcript
432 quantification and downstream analyses, including cell segmentation, cell quality, and biological
433 interpretation. All these factors must be considered when designing iST experiments.

434 There are significant workflow differences between the different platforms which factor
435 into the choice of method. Cutting samples onto MERSCOPE coverslip is more difficult than on
436 standard microscope slides. The total hands-on time for running a slide on Xenium is 2-3 days
437 compared to 5-7 days for MERSCOPE and 2 days on CosMx. We found that MERSCOPE and
438 CosMx are well set up for batch processing in the wet lab, either due to built-in pause points or the
439 instrument's ability to run multiple samples. Xenium is limited for batch processing by a need for
440 a separate thermocycler for each slide pair processed in parallel. After staining, selecting regions
441 of interest (ROIs) presented a surprising challenge for some systems: the Xenium platform could
442 readily image the entire slide as a single ROI which easily covered entire TMAs, but the
443 MERSCOPE ran into a 1cm² imaging area limit which meant cores in the addressable region were
444 left unimaged, while the CosMx workflow required a demanding manual selection of ROIs for
445 each core. These factors are likely to change as each company updates its protocol, but currently,
446 Xenium offers the shortest and least hands-on workflow.

447 From a technical perspective, we analyzed each resulting dataset with a combination of
448 manufacturer recommended processes for each platform and computational tools that can be
449 implemented by the user downstream. These pipelines each result in count matrices and detected
450 transcripts that can be analyzed using a whole suite of emerging tools. For our purposes, when
451 analyzed at a core level to abrogate the effects of individual cell-segmentation performance, we
452 found that the total number of transcripts varied substantially across iST platform, with Xenium
453 yielding the highest number of transcripts captured followed by CosMx. Indeed, this trend held
454 when normalized for the number of cores imaged and on a per cell basis per area. When this
455 analysis was also restricted to shared genes, we also found that Xenium consistently had higher
456 expression levels across each tissue type, with no clear differences between performance on either
457 tumor or normal tissue.

458 Using a pseudo-bulk approach, again at the core level, we assessed overall correlation,
459 reproducibility, and sensitivity of each platform. We found high correlation between replicates of
460 the same patient, suggesting that there is high reproducibility across technical replicates on each
461 platform. This is important to consider since cost or input material availability can be prohibitive
462 to implementing experimental designs that leverage technical replicates—though additional tissue
463 may still be valuable for powering cell-cell interaction analysis. We additionally found high
464 correlation on a gene-by-gene basis between MERSCOPE and Xenium platforms. Xenium and
465 MERSCOPE also showed consistently high specificity across tissue types. CosMx displayed a
466 characteristic upward curve when compared to MERSCOPE or Xenium on a gene-by-gene basis,
467 indicating more frequent calls in the lower expression regime. This, coupled with the lower
468 specificity across several tissues for CosMx and the high false discovery rate, suggest that CosMx
469 is prone to errors in calling lowly expressed genes. Finally, Xenium had the highest sensitivity

470 across tissues. CosMx and MERSCOPE both detected fewer transcripts than Xenium.
471 MERSCOPE outperformed CosMx in the higher quality (as judged by relative performance across
472 all platforms) tumor TMA but underperformed it in lower quality normal tissue TMA. In general,
473 our analyses also suggest similar performance within a given platform across a vast array of tissue
474 types assayed here. We note that given the small number of replicates from each tissue, particularly
475 in the normal tissue, we stop short of making blanket statements about relative performance across
476 a particular tissue type. The data suggests, instead, that Xenium and MERSCOPE provide more
477 reliable true-positive signals of lowly expressed genes and that Xenium's overall performance is
478 less dependent on sample input quality than the other two platforms. MERSCOPE, especially,
479 appears to be particularly sensitive to sample input, highlighting the importance of prescreening
480 RNA integrity according to manufacturer instructions.

481 When we compared each dataset to existing RNA-seq datasets, we found comparable
482 correlation of pseudo-bulk data to RNA-seq data from GTEx or the TCGA across each panel and
483 platform. However, the presence of a characteristic upswing for CosMx, even when comparing to
484 orthogonal data, further shows that there is a higher false positive rate for lower expression level
485 genes in CosMx data. This upswing could be explained by the absence of probing genes in a
486 particular tissue in a larger panel. However, the Xenium multi tissue panel also includes genes not
487 expressed in breast and lung but does not show a similar upswing. Thus, a more likely
488 interpretation is that the CosMx is prone to a high FDR at the low expression regime. This could
489 also suggest that the CosMx transcript counts and detected gene numbers may be slightly inflated
490 by false discoveries.

491 From a tissue-specific expression perspective, Xenium showed a distinct expression
492 pattern of key tissue-markers, whereas CosMx and MERSCOPE did not. Additionally,

493 MERSCOPE and CosMx consistently showed expression of known tissue markers in unexpected
494 tissue types. This could be partly explained by an overall low performance on this particular normal
495 tissue TMA for MERSCOPE due to RNA quality. This performance difference could be
496 problematic for studies that are designed to compare tissue-specific factors. For studies whose
497 main biological variables of interest are within the same tissue, factors like sensitivity, specificity,
498 and panel availability may be a more important guide for iST experimental design.

499 A significant advantage of spatial transcriptomics data is the ability to map expression in
500 single cells. We compared each platform on a cell-level basis by assessing cell identification and
501 cell clustering. Overall, it appears that the out-of-the-box segmentation from Xenium performs
502 poorly in terms of drawing cell boundaries specific to a single cell, while MERSCOPE and CosMx
503 much more closely match cell boundaries. This did not appear to differ on a tissue-by-tissue basis,
504 thus, is likely inherent to the overall approach used by each platform. After applying an expression
505 level filter, Xenium overall retained the highest number of cells across various filtering
506 stringencies. Despite Xenium's cell boundaries not clearly matching nuclei, both it and
507 MERSCOPE were able to effectively separate cells from different lineage markers, as judged by
508 finding minimal coexpression of disjoint markers, while CosMx showed more double positive
509 cells (out of, it should be noted, fewer cells expressing the target genes overall).

510 To determine whether clearer identification of lineage markers resulted in improved ability
511 to identify cell types, we performed clustering analyses specifically in the breast tissue and breast
512 cancer samples. We note that we used the full panel, not only the shared genes, when performing
513 these clustering analyses. Xenium allowed for identification of all major cell lineages in the breast
514 when compared to several reference breast atlases. Both the global and tissue clustering results
515 show that CosMx is also able to recognize the major cell types, but cannot identify cell subtypes.

516 Additionally, since the cluster-enriched genes do not correspond to well-known markers, probably
517 due to the low expression caused by low sensitivity and specificity, cell type annotation was
518 particularly difficult. Lastly, despite lower transcript counts and fewer cells, MERFISH still
519 successfully identified cell groups, capturing the patterns seen in other platforms. These
520 differences in cell typing, can also be attributed to the differential performance of cell segmentation
521 pipelines^[37,38 39,40]. Since all platforms provide the underlying DAPI stain and morphology images
522 (in the case of CosMx and MERSCOPE) it is likely that segmentation performance could be
523 improved on a sample-by-sample or tissue-type-by tissue-type basis. Future work should seek to
524 assess cell segmentation tools and their performance across data from each platform to help inform
525 the choice of analytical method where needed.

526 Plex is an important factor in ST experiments which we have not explicitly considered. The
527 kinds of questions that may be answered by a 1,000-plex panel are clearly different than those
528 answered by a 300-plex panel, offering more opportunities to explore intra- and intercellular
529 signaling interactions. Thus, we note that for the right question, the higher false positive rates and
530 lower sensitivities of CosMx relative to Xenium could be tolerated for a broader coverage of the
531 biology. On the other hand, the fully configurable nature of Xenium and MERSCOPE panels could
532 be better suited for branches of biology not well sampled by the 1,000 plex CosMx panel. We
533 recommend subsampling existing atlas data to determine whether the gene set which can be studied
534 will be sufficient to cluster the cell types of interest and identify the necessary biological programs.
535 We note that each of the manufacturers has publicly stated plans to grow their product offerings
536 to increasing panel sizes.

537 There are several limitations of our study. While we attempted to match time post slicing,
538 the unintentional acquisition of MERSCOPE tissues at thinner thicknesses meant that the rerun

539 MERSCOPE data had a longer time on the slide than other panels. However, the fact that the
540 increase in counts in the rerun matched the increase in imaging volume, and the fact that Xenium
541 runs showed stable expression levels over time suggests that this contribution was minimal.
542 Additionally, our panel design for MERSCOPE required the removal of genes so the panel was
543 compatible with all tissues, lowering the plexity slightly. This could have compromised
544 MERSCOPE's ability to identify cell types relative to Xenium.

545 Most importantly, we only attempted to compare the performance of iST platforms under
546 typical use cases for clinical samples obtained from archival biobanks. Our results don't
547 necessarily extend to non-human samples, frozen samples, and even FFPE samples which have
548 been extensively validated for high RNA integrity. Indeed, there have been reports that
549 MERSCOPE, in previous studies of the mouse brain, shows comparable or even superior results
550 to those reported by 10x Xenium^[41]. Given the large change in data quality between the normal
551 and tumor TMA, we cannot exclude the possibility that in the highest quality samples MERSCOPE
552 would provide higher transcript numbers, with the associated downstream benefits relative to
553 Xenium and CosMx. However, the current guidance of DV₂₀₀>0.6 restricts studies to the upper
554 regime sample quality and limits archival investigations.

555 Despite these limitations, our overall interpretation of these results is that amplification of
556 RNA signal is especially important for recovery of transcript counts by iST in low-quality samples
557 where RNA may be highly degraded and fewer landing sites are available for probes. Platforms
558 (such as Xenium) which rely on small numbers of landing sites and are subsequently heavily
559 amplified are robust to RNA degradation and are thus more broadly compatible with a broad range
560 of samples. On the other hand, when sample quality is high (as in some of our tumor samples) the

561 gap between amplified and unamplified platforms' performance closes and most platforms can
562 yield useful data for subsequent downstream spatial analysis.

563 **Methods**

564 **Sample choice and TMA construction**

565 Two TMAs were constructed using FFPE clinical discards at Brigham and Women's
566 Hospital Pathology Core and were acquired with a waiver of consent for non-sequencing based
567 readouts under IRB 2014 P 001721. The samples included:

568 1. A tumor TMA of 170 cores, 0.6 mm in diameter, including a variety of cancer samples
569 and healthy lymphoid tissue as a positive staining control. The TMA samples were
570 selected from samples previously characterized by ImmunoProfile and were selected
571 to encompass both high and low levels of the biomarkers in the ImmunoProfile panel
572 [CD8, PD-1, PD-L1, Foxp3, tumor marker (Cytokeratin, Sox10, or PAX8)].
573 Annotations were performed by KF and SR based on H&E and immunofluorescence
574 staining. Cores included both tumor and healthy control annotation, though for the
575 purpose of this study, all were combined under their tumor label. Tumors were also
576 chosen to be a mixture of *PD-L1* high and *PD-L1* low, a parameter to be analyzed at a
577 future date. This TMA had previously been studied by both H&E, and several highly
578 multiplexed immunostaining approaches, and was known to be of high morphological
579 integrity.

580 2. A normal TMA of 45 cores 1.2 mm in diameter representing a broad range of normal
581 tissues. Samples were sourced from the same patient in either duplicate or triplicate.

582 This TMA was chosen for the breadth of tissue lineages included and the relatively
583 large core size.

584 All samples were fully de-identified before assembly into TMAs. The breakdown of the number
585 of samples per tissue and the number of cores per tissue is included in **Supplementary Table 1-**
586 **2.**

587 **Preparation of sequential sections**

588 Sequential sections were prepared according to manufacturer instructions (“Tissue
589 Preparation Guide Demonstrated Protocol CG000578” for Xenium, “91600112 MERSCOPE User
590 Guide Formalin-Fixed Paraffin-Embedded Tissue Sample Preparation RevB” for Vizgen, and
591 “MAN-10159-01CosMx SMI Manual Slide Preparation Manual” for CosMx) at the Brigham and
592 Women’s Hospital Pathology Core. Prior to collecting samples, ~50 µm of each TMA were faced
593 off to reach deeper into the sample where RNA integrity was likely higher. 5 µm sequential
594 sections were then collected, floated in a 37°C water bath, and adhered to Xenium slides (10x, PN
595 1000460), Vizgen FFPE coverslips (Vizgen, PN 10500102), or standard Superfrost+ slides for
596 CosMx (Leica BOND PLUS slides, Leica Biosystems S21.2113.A). TMAs were sliced as close to
597 the center of the active area as possible for each platform. Samples were baked at 42°C for 3 hours
598 for Xenium, 55 °C for 15 minutes for MERSCOPE, and 60°C for 16 hours for CosMx. Sections
599 were stored according to manufacturer instructions prior to processing, with 10x Xenium stored in
600 a desicator at room temperature, Vizgen MERSCOPE coverslips stored at -20°C, and NanoString
601 CosMx slides stored at 4°C. Samples for 10x Xenium and Vizgen MERSCOPE were brought to
602 the Spatial Technology Platform at the Broad Institute for processing, while samples for
603 NanoString CosMx were processed at the Wei lab at Brigham and Women’s Hospital.

604

605 **Vizgen MERSCOPE probe selection**

606 Pre-designed probe panels from Vizgen were not available at the time of the experiment.
607 Therefore, we ordered custom gene panels to match the pre-released gene panels from 10x for the
608 human breast and human lung panels. Gene lists were uploaded to the Vizgen panel design portal
609 and were checked against all profiled tissues, removing genes that were overexpressed in any
610 individual tissue based on Vizgen's design guidelines (FPKM > 900), and ensuring that the total
611 panel FPKM did not exceed the allowed limit in any individual sample type. Panels were
612 manufactured at the 300 gene scale as custom panels BP0892 and BP0893. The final gene lists, for
613 all three iST modalities are available in **Supplementary Table 3**.

614

615 **Vizgen MERSCOPE data acquisition**

616 MERSCOPE samples were imaged according to manufacturer protocol "9160001
617 MERSCOPE Instrument User Guide RevF". Samples were processed in two batches, the first of
618 four samples, two of each TMA and with each library prepped in parallel; and a follow up sample
619 of each TMA re-run with the breast panel. Samples were first hybridized with anchoring probes
620 overnight before being embedded in a polyacrylamide gel. Samples were incubated for two hours
621 with a digestion solution at 37°C and then overnight at 47°C overnight in a detergent clearing
622 solution and proteinase K to remove native proteins while the anchoring probes kept nucleic acids
623 bound to the gel. After clearing, samples were additionally photobleached using Vizgen's
624 MERSCOPE Photobleacher for three hours at room temperature in the clearing solution. Samples
625 were hybridized with encoding probes and a cell boundary stain (PN 10400118) and then imaged
626 with imaging kits (PN 10400005). Samples were stored at 37°C in clearing solution after
627 hybridization and before final imaging. After an initial examination of the data, a second batch of

628 both TMAs were run a second time with the human breast panel, increasing the set imaging capture
629 thickness from 5 µm to 10 µm to capture more tissue from cores that had lifted during the gel
630 embedding process. Data was processed on premises through the standard Vizgen workflow to
631 generate cell by gene and transcript by location matrices. We segmented the data with a built-in
632 Cellpose method on the most accurate looking cell boundary stain.

633

634 **10x Xenium data acquisition**

635 10x Xenium samples were processed in three batches according to manufacturer protocols
636 “Probe Hybridization, Ligation & Amplification, User Guide CG0000582” and “Decoding &
637 Imaging, User Guide CG000584”. Samples were stained utilizing 10x’s predesigned Human
638 Breast (10x, PN 1000463), Human Multi-Tissue and Cancer (10x, PN 1000626), and Human Lung
639 panels (10x, PN 1000601), as they became available from the manufacturer. Slides for both TMAs
640 were processed in pairs according to which probe library they were receiving. Slides were stained
641 with a Xenium imaging kit according to manufacturer instructions (10x, PN 1000460). Briefly,
642 padlock probes were incubated overnight before rolling circle amplification and native protein
643 autofluorescence was reduced with a chemical autofluorescence quencher. Slides were processed
644 on a 10 Xenium Analyzer, with ROIs selected to cover the entire TMA region. Data was processed
645 on premises through the standard 10x workflow to generate cell by gene and transcript by location
646 matrices.

647

648 **NanoString CosMx**

649 NanoString CosMx samples were prepared with one 1000 plex panel. Samples were
650 hybridized with probes and stained with cell markers. Samples were loaded onto the CosMx SMI

651 at the same time for imaging, during which branched fluorescent probes were hybridized onto the
652 samples to amplify the signal above the background.

653 NanoString CosMx samples were prepared with Human Universal Cell Characterization
654 1000 Plex Panel (part number 122000157) according to manufacturer protocol “MAN-10159-01
655 CosMx SMI Manual Slide Preparation Manual”. Firstly, slides were baked at 60°C overnight for
656 better tissue adherence. After baking, slides were treated sequentially with deparaffinization, target
657 retrieval (15 min at 100°C), permeabilization (3µg/mL proteinase K, 15 min at 40°C), fiducials
658 application, post-fixation, NHS-acetate application and then hybridized with denatured probes
659 from universal panel and default add-on panel. After *in situ* hybridization (18 hours at 37°C), slides
660 were washed and incubated with DAPI (15 min at RT) and marker stain mix (with *PanCK*, *CD45*,
661 *CD68* and cell segmentation marker *CD298/B2M*). Slides were washed and loaded onto the
662 CosMx SMI for UV bleaching, imaging, cycling and scanning. Raw images were decoded by
663 default pipeline on Atomx SIP (cloud-based service). Machine: CosMx_0020. Serial Number:
664 INS2301H0020

665 **Data preprocessing**

666 After data acquisition, the resulting outputs were uploaded to a Google bucket associated
667 with a terra.bio Workspace for distribution and follow on analysis.

668 To facilitate standardized data formatting and subsequent analytical processes, we built a
669 data ingestion pipeline with the following objectives: a) to grab cell-level and transcript-level
670 data from diverse platforms and normalize the data structure; b) to tag each cell and transcript
671 with essential metadata including tissue type, tumor status, *PD-L1* status, among others
672 (**Supplementary Fig. 6**); and c) to transform the data into various formats tailored to the
673 requirements of particularized analyses. Specifically, to tag the data, core centers in the TMA

674 were manually identified using DAPI images (Xenium) or cell metadata that contains global
675 coordinates (MERSCOPE and CosMx) using QGIS(version:3.16.10-Hannover). Cells or
676 transcripts within a specified radius were then labeled with core metadata via spatial joining
677 (implemented by GeoPandas, version:0.13.0). In instances where cores are in close proximity or
678 when a uniform radius cannot be applied effectively, we manually generated the core boundary
679 masks.

680

681 **Reproducibility**

682 To evaluate panel to panel reproducibility we summed the expression level of shared
683 genes between indicated panels (breast vs. multi-tissue and breast vs. lung panels from Xenium
684 and breast vs. lung panels from MERCOPe) over an individual core and plotted all cores present
685 in each panel, before calculating a Pearson's correlation. The format of the data used is shown in
686 **Supplementary Table 10**. To evaluate core to core reproducibility, the individual gene counts of
687 core 1 were plotted against those of core 2 and a Pearson's r correlation was calculated.

688 **On target rates and false-discovery measurements**

689 To compare across panels and platforms, we subset all datasets to include only cores
690 assayed in all runs. The fraction of on-target barcodes was calculated as a percentage of all
691 transcripts corresponding to genes relative to the total number of calls (including negative
692 control probes and unused barcodes or blank barcodes). These measurements were performed on
693 individual cores and averaged across all cores of the same tissue type.

694 Because the difference in relative numbers of controls and target barcodes across
695 different platforms, we adopted the false discovery rate (FDR) calculation to evaluate the
696 specificity in a more normalized way (**Fig. 2f-g**). We calculated the FDR of platform p panel m
697 data in tissue t using the following equation and cell level data (**see example in Supplementary**
698 **Table 11**):

$$699 FDR(\text{negative control probes})_{p,m}^t = \text{mean} \left(\frac{\sum_j neg_{jn}}{\sum_i g_{in} + \sum_j neg_{jn}} \times \frac{I}{J} \times \% \right), \quad n = \{1, \dots, N\}$$

700 Where N is the total number of cores that belong to tissue type t , I is the total number of unique
701 genes, J is the total number of negative control probes, g_{in} is the gene expression of gene i in
702 core n , neg_{jn} is the total calls negative control probe j in core.

703 Since MERSCOPE does not include negative control probes, FDR was recalculated by
704 substituting negative control with blank barcodes (**Fig. 2f**) using the following equation:

$$705 FDR(\text{blank barcodes})_{p,m}^t = \text{mean} \left(\frac{\sum_l blank_{ln}}{\sum_i g_{in} + \sum_l blank_{ln}} \times \frac{I}{L} \times \% \right), \quad n = \{1, \dots, N\}$$

706 Where N is the total number of cores that belong to tissue type t , I is the total number of unique
707 genes, L is the total number of unused barcodes or blank barcodes, g_{in} is the gene expression of
708 gene i in core n , $blank_{ln}$ is the total calls of unused barcode or blank barcode l in core n ,

709 specifically, we used “BLANK” for Xenium, “Blank” for MERSCOPE, and “SystemControl”
710 for CosMx. We only used the data from matched cores, so N is same for different platform p .

711

712 **Sensitivity comparison**

713 Sensitivity was measured by the percentage of the total number of unique genes detected
714 above noise level, where the noise was estimated as two standard deviation above average
715 expression of the negative control probes.

716

717 **Orthogonal RNA-Seq concordance analysis**

718 RNA TCGA cancer sample gene data summarizes 7,932 samples from 17 different cancer
719 types, and it provides FPKM for each gene documented. We used all samples which were
720 annotated as BRCA (Breast cancer), BLCA (Bladder cancer), COAD and READ (colorectal
721 cancer), HNSC (head and neck squamous cell carcinoma), LUAD and LUSC (non-small cell lung
722 cancer), SKCM (melanoma), and OV (ovarian cancer). For GTEx, we selected the tissue types
723 matching the annotation in our normal tissue TMA. For each panel, the genes probed by iST were
724 averaged across all patients with the matching tissue label from the RNA-seq database.

725 To get pseudo-bulked iST values, the expression level of each gene in each core was normalized
726 to the sum of all genes in that core and scaled by 100,000. We then averaged these scaled pseudo-
727 bulk expression values across cores and plotted them against the averaged FPKMs from reference
728 RNA-seq data sets.

729

730 **Tissue marker enrichment analysis**

731 To determine the assay's ability to specifically identify known lineage markers, we focused
732 on the normal tissue TMA profiled with multi-tissue panel of Xenium, breast panel of MERSCOPE,
733 and 1K panel of CosMx. We selected genes with known canonical expression patterns using based
734 on transcriptomics data from GTEx. If a gene had 20-fold higher expression in a specific tissue
735 than every other tissue combined, this gene was considered to be a tissue marker and was used for
736 assessing specificity for each platform. Counts for each gene were normalized to the total counts
737 within the core, and then the Z-score of this gene across tissue types was plotted in a heatmap **Fig.**
738 **3e**. We calculated average expression of a gene across cores of the same tissue type and normalized
739 to the total averaged expression of all genes. Z-scores were calculated with the mean and standard
740 deviation across all averaged genes.

741

742 **Evaluation of cell segmentation performance**

743 In the absence of ground truth data, we conducted a comparative analysis of cell counts,
744 cell areas, coexpression across various platforms and panels, utilizing the segmentation results
745 supplied by each respective company. To facilitate comparison, cell counts were normalized to a
746 consistent area of 1000 μm^2 . Both cell count and cell area were then delineated at two distinct
747 levels of detail: a consolidated assessment encompassing all tissue types (see **Fig. 4b-c**), as well
748 as a segregated evaluation by individual tissue types (refer to **Supplementary Table 6-7**). To
749 evaluate the biological performance of the segmentation, we plotted coexpression plots of gene
750 pairs that are mutually exclusive including *CD3e* vs. *CD19*, *CD4* vs. *CD8*, and *CD3e* vs.
751 *EPCAM*. We pooled all the filtered cells from matched cores and all available panels of each
752 platform, dropped cells which do not express either gene, plotted the expression of one gene

753 against the other, and converted the scatter plot to a 2D histogram showing cell numbers in each
754 co-expression bin (**Fig. 4g**).

755

756 Cells per area quantification

757 Segmented cells were aggregated by TMA cores. For Xenium and MERSCOPE data, the
758 estimation of tissue area was performed by calculating the area of a discernible circle, utilizing
759 respective radius of 0.3 μm and 0.6 μm for tumor and normal TMA samples. Conversely, for the
760 CosMx dataset, the tissue area estimation was approached differently due to its square-like data
761 presentation, a result of the FOV selection process. Here, the tissue area was deduced by
762 multiplying the number of FOVs covered by each core with the area of a single FOV.

763 Clustering

764 For cell filtering, cells with less than 10 transcript counts in MERFISH and Xenium
765 datasets were removed, and cells with less than 20 transcript counts in CosMx datasets were
766 removed. We followed standard processes to then cluster and annotate cell types across each
767 dataset using Scanpy^[42]. Briefly, data was normalized and scaled, dimensionality reduction was
768 performed and cell clusters were identified^[43, 44]. To identify the cell type for each cluster, we used
769 a t-test to find the markers for each Leiden cluster and annotated them according to previous
770 literature^[29-36]. These are some of the example markers used for cell type annotation: in breast
771 samples, PIGR and KIT for alveolar cells, for B cells, KRT5, DST, and MYLK for basal cells,
772 LUM, MMP2 and CXCL12 for fibroblast, etc. Heatmaps of the top 3 markers for each cluster are
773 drawn for each dataset from all three panels (refer to **Supplementary Figure 5a-c**). For datasets
774 that showed batch effect with patients, Harmony was used to remove this variance^[45]. Correlation

775 heatmaps were generated over overlapping genes that exist in both datasets, and the Pearson
776 correlation coefficient was calculated.

777

778 **Acknowledgment**

779 We thank Nir Hacohen, Ilya Korsunsky, Roopa Madhu, and Ksenia Anufrieva for helpful
780 discussions, as well as Patricia Rogers and Natan Pierete for assistance with the 10x Xenium data
781 acquisition. We appreciate 10x Genomics, Vizgen, and NanoString Technologies for reviewing
782 data and analyses for quality. This work is supported by a Broad Institute SPARC grant and by a
783 Brigham and Women's Hospital Department of Medicine - Broad Institution collaborative
784 research Award. K.W. is supported by a NIH-NIAMS K08AR077037, a Burroughs Wellcome
785 Fund Career Awards for Medical Scientists, and a Doris Duke Charitable Foundation Clinical
786 Scientist Development Award. B.A.G is supported in part through the Geisel School of Medicine
787 at Dartmouth's Center for Quantitative Biology through a grant from the National Institute of
788 General Medical Sciences (NIGMS, P20GM130454) of the NIH.

789

790 **Author contributions**

791 Conceptualization: A.Y., S.F., tissue-microarray construction: K.F., K.P., T.B., S.R.,
792 pathological annotation: K.P., S.R., gene selection: A.Y., S.F., Xenium and MERSCOPE data
793 acquisition: J.N., CosMx data acquisition: C.G., M.T., K.W., analysis: H.W., R.H., B.G., S.F.,
794 figure generation: H.W., R.H., B.G., S.F., writing original draft: H.W., R.H., J.N., B.G., S.F., draft
795 reviewing and editing: H.W., R.H., B.G., S.F., supervision: B.G., S.F., funding acquisition: S.F.
796 K.W.

797

798 **Data and Code Availability**

799 Cell-level data and gene-level data will be made available at the time of final publication.

800 All code used in this manuscript for data processing and analysis will be made available on

801 GitHub prior to final publication.

802 **Declaration of interests**

803 All authors declare that they have no conflicts of interest.

804

805 **References**

- 806 1. Chen W.T., Lu A. Croissants K. et al. Spatial Transcriptomics and In Situ Sequencing to
807 Study Alzheimer's Disease. *Cell.* 182 (4), 976–991 (2020).
- 808 2. Hunter, M.V., Moncada, R., Weiss, J.M. et al. Spatially resolved transcriptomics reveals
809 the architecture of the tumor-microenvironment interface. *Nat Commun* 12, 6278 (2021).
- 810 3. Lein E, Borm LE, Linnarsson S. The promise of spatial transcriptomics for neuroscience
811 in the era of molecular cell typing. *Science.* 2017 Oct 6;358(6359):64-69.
- 812 4. Lewis SM, Asselin-Labat ML, Nguyen Q, et al. Spatial omics and multiplexed imaging to
813 explore cancer biology. *Nat Methods.* 2021 Sep;18(9):997-1012.
- 814 5. Rao, A., Barkley, D., França, G.S. et al. Exploring tissue architecture using spatial
815 transcriptomics. *Nature* 596, 211–220 (2021).
- 816 6. Haque, A., Engel, J., Teichmann, S.A. et al. A practical guide to single-cell RNA-
817 sequencing for biomedical research and clinical applications. *Genome Med* 9, 75 (2017).
- 818 7. Williams, C.G., Lee, H.J., Asatsuma, T. et al. An introduction to spatial transcriptomics for
819 biomedical research. *Genome Med* 14, 68 (2022).

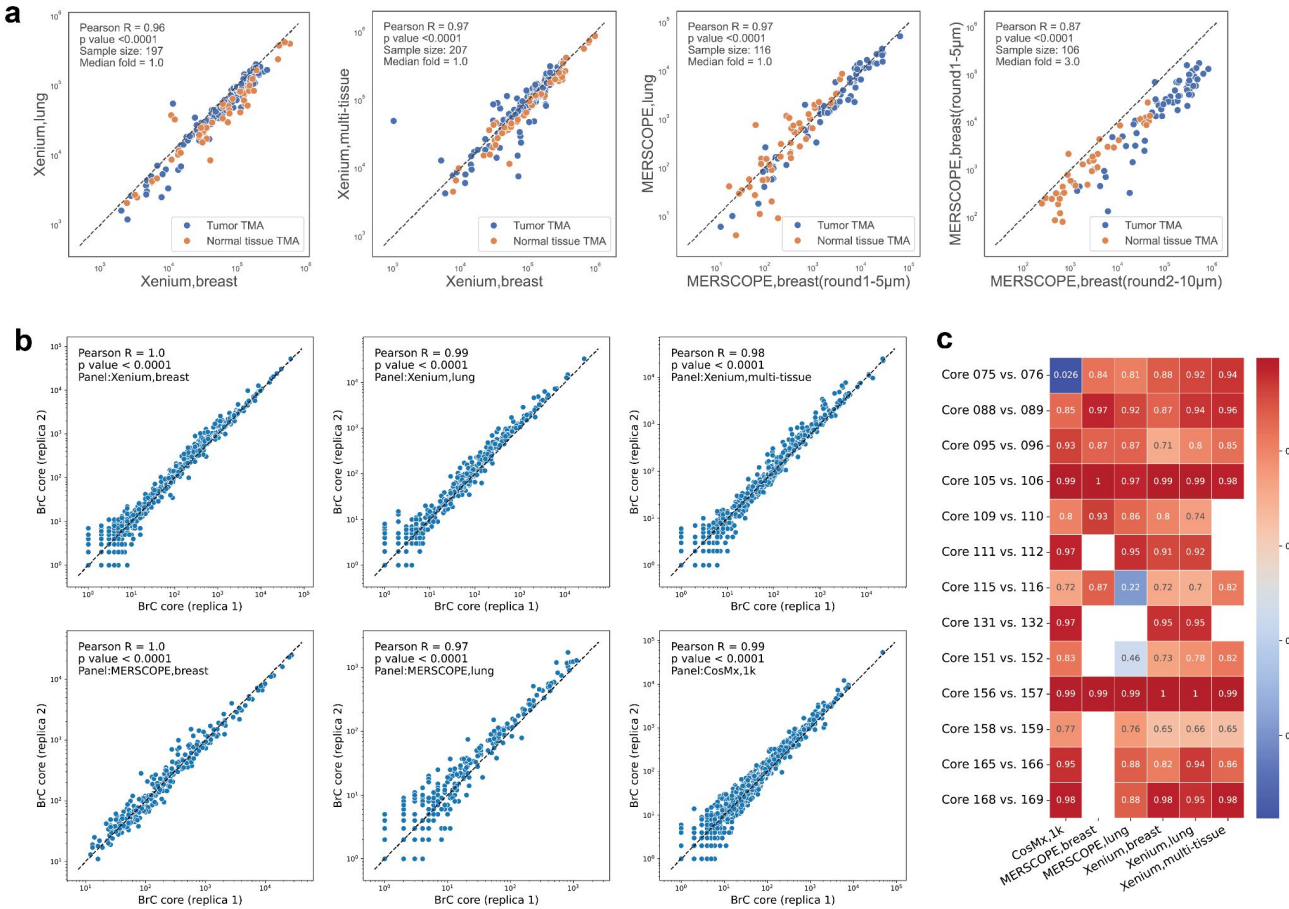
- 820 8. Tian, L., Chen, F. & Macosko, E.Z. The expanding vistas of spatial transcriptomics. *Nat*
821 *Biotechnol* 41, 773–782 (2023).
- 822 9. Janesick A., Shelansky R., Andrew D.G., et al. High resolution mapping of the breast
823 cancer tumor microenvironment using integrated single cell, spatial and insitu analysis of
824 FFPE tissue. *bioRxiv* 2022.10.06.510405
- 825 10. He S., Bhatt R., Birditt B., et al. High-plex multiomic analysis in FFPE tissue at single-
826 cellular and subcellular resolution by spatial molecular imaging. *bioRxiv*
827 2021.11.03.467020
- 828 11. Moffitt, J. R. et al. Molecular, spatial, and functional single-cell profiling of the
829 hypothalamic preoptic region. *Science* 362, eaau5324 (2018).
- 830 12. Du J., Yang Y.C., An Z.J., et al. Advances in spatial trasnciptomics and related data
831 analysis strategies. *J Transl Med.* 2023; 21: 330.
- 832 13. Phan, H.V., van Gent, M., Drayman, N. et al. High-throughput RNA sequencing of
833 paraformaldehyde-fixed single cells. *Nat Commun* 12, 5636 (2021).
- 834 14. Xu, Z., Zhang, T., Chen, H. et al. High-throughput single nucleus total RNA sequencing
835 of formalin-fixed paraffin-embedded tissues by snRandom-seq. *Nat Commun* 14, 2734
836 (2023).
- 837 15. Gnanapragasam VJ. Unlocking the molecular archive: the emerging use of formalin-fixed
838 paraffin-embedded tissue for biomarker research in urological cancer. *BJU Int.* 2010
839 Jan;105(2):274-8.
- 840 16. Matsunaga H., Arikawa K., Yamazaki M., et al. Reproducible and sensitive micro-tissue
841 RNA sequencing from formalin-fixed paraffin-embedded tissues for spatial gene
842 expression analysis. *Sci Rep* 12, 19511 (2022).

- 843 17. Kok Hao Chen et al. Spatially resolved, highly multiplexed RNA profiling in single
844 cells. *Science* 348, aaa 6090 (2015).
- 845 18. Walsh, L.A., Quail, D.F. Decoding the tumor microenvironment with spatial technologies.
846 *Nat Immunol* 24, 1982–1993 (2023).
- 847 19. Tomczak K., Czerwinska P., Wiznerowicz M. The cancer genome atlas (TCGA): an
848 immeasurable source of knowledge
- 849 20. GTEx Consortium. Genetic effects on gene expression across human tissues. *Nature* 550,
850 204–213 (2017).
- 851 21. Junttila S., Smolander J., Elo L., et al. Benchmarking methods for detecting differential
852 states between conditions from multi-subject single-cell RNA-seq data. *Briefings in
853 Bioinformatics*, Volume 23, Issue 5, Sep. 2022.
- 854 22. Zimmerman S. M., Fropf R., Kulasekara B. R., et al. Spatially resolved whole
855 transcriptome profiling in human and mouse tissue using digital spatial profiling. *Genome
856 Res.* 2022 Oct;32(10):1892-1905.
- 857 23. Trevethan. R. Sensitivity, specificity and predictive values: foundations, liabilities, and
858 pitfalls in research and practice. *Front Public Health*. 2017 Nov 20;5:307.
- 859 24. He S, Bhatt R, Brown C. et al. High-plex imaging of RNA and proteins at subcellular
860 resolution in fixed tissue by spatial molecular imaging. *Nat Biotechnol*. 2022
861 Dec;40(12):1794-1806.
- 862 25. Garrido-Trigo A, Corraliza AM, Veny M et al. Macrophage and neutrophil heterogeneity
863 at single-cell spatial resolution in human inflammatory bowel disease. *Nat Commun*. 2023
864 Jul 26;14(1):4506. doi: 10.1038/s41467-023-40156-6. PMID: 37495570; PMCID:
865 PMC10372067.

- 867 26. Nieto P., Elosua-Nayes M., Trincado J. L., et al. A single-cell tumor immune atlas for
868 precision oncology. *Genome Res.* 2021 Oct; 31(10): 1913–1926.
- 869 27. Elmentait R., Conde C. D., Yang L., et al. Single-cell atlases: shared and tissue-specific
870 cell types across human organs.
- 871 28. Heumos L., Schaar A. C., Lance C., et al. Best practices for single-cell analysis across
872 modalities. *Nat Rev Genet* 24, 550–572 (2023).
- 873 29. Kumar, T., Nee, K., Wei, R. et al. A spatially resolved single-cell genomic atlas of the adult
874 human breast. *Nature* 620, 181–191 (2023).
- 875 30. Gray G.K., Li C.M., Rosenbluth J.M. et al. A human breast atlas integrating single-cell
876 proteomics and transcriptomics. *Developmental Cell*, Volume 57, Issue 11, 2022.
- 877 31. Reed A.D., Pensa S., Steif A. et al. A human breast cell atlas mapping the homeostatic
878 cellular shifts in the adult breast. *bioRxiv* 2023.04.21.537845
- 879 32. Travaglini K.J., Nabhan A.N., Penland L. et al. A molecular cell atlas of the human lung
880 from single-cell RNA sequencing. *Nature* 587, 619–625 (2020).
- 881 33. Sikkema, L., Ramírez-Suástequi, C., Strobl, D.C. et al. An integrated cell atlas of the lung
882 in health and disease. *Nat Med* 29, 1563–1577 (2023).
- 883 34. Wu, S.Z., Al-Eryani, G., Roden, D.L. et al. A single-cell and spatially resolved atlas of
884 human breast cancers. *Nat Genet* 53, 1334–1347 (2021).
- 885 35. Dave A., Charytonowicz D., Francoeur N. et al. The breast cancer single-cell atlas: defining
886 cellular heterogeneity within model cell lines and primary tumors to inform disease
887 subtype, stemness, and treatment options. *Cell Oncol (Dordr)*. 2023 Jun;46(3):603-628.
- 888 36. Yeo S.K., Zhu X., Okamoto T. et al. Single-cell RNA sequencing reveals distinct patterns
889 of cell state heterogeneity in mouse models of breast cancer. *eLife* 9:e58810.

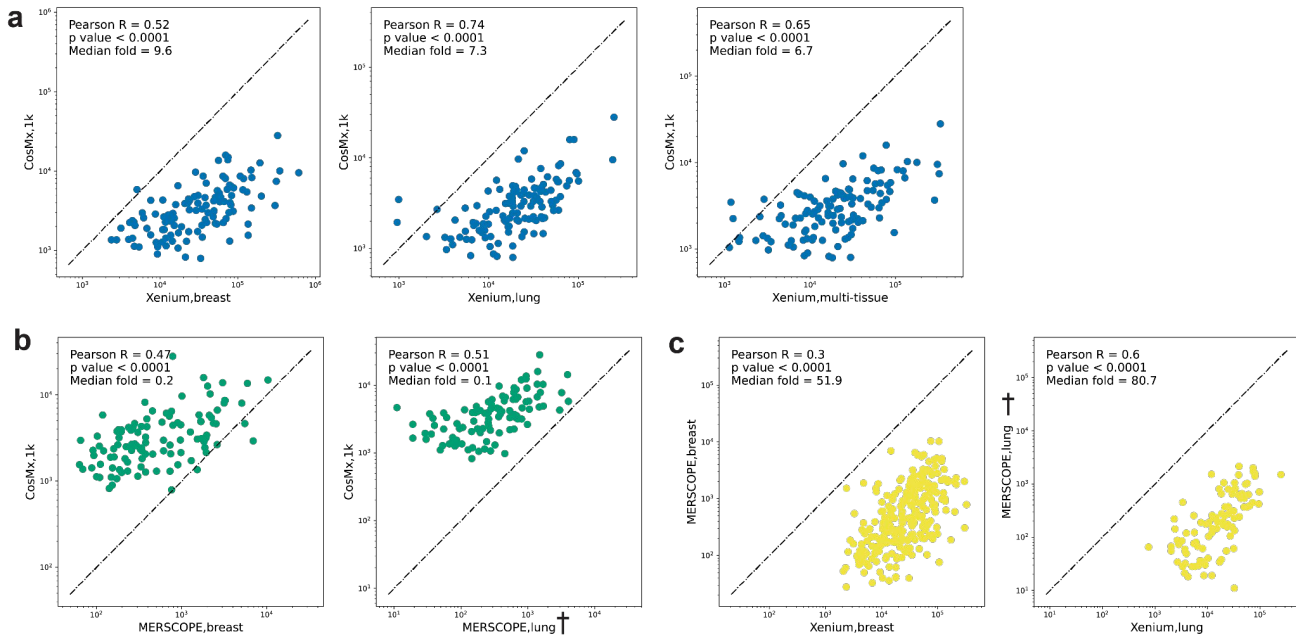
- 890 37. Greenwald, N.F., Miller, G., Moen, E. et al. Whole-cell segmentation of tissue images with
891 human-level performance using large-scale data annotation and deep learning. *Nat*
892 *Biotechnol* 40, 555–565 (2022).
- 893 38. Stringer, C., Wang, T., Michaelos, M. et al. Cellpose: a generalist algorithm for cellular
894 segmentation. *Nat Methods* 18, 100–106 (2021).
- 895 39. Petukhov, V., Xu, R.J., Soldatov, R.A. et al. Cell segmentation in imaging-based spatial
896 transcriptomics. *Nat Biotechnol* 40, 345–354 (2022).
- 897 40. Chen, H., Li, D. & Bar-Joseph, Z. SCS: cell segmentation for high-resolution spatial
898 transcriptomics. *Nat Methods* 20, 1237–1243 (2023).
- 899 41. Marco Salas, S., Czarnewski, P., Kuemmerle, L. B., Helgadottir, S., Mattsson Langseth,
900 C., Tiesmeyer, S., ... & Nilsson, M. (2023). Optimizing Xenium In Situ data utility by
901 quality assessment and best practice analysis workflows. *bioRxiv*, 2023-02.
- 902 42. Wolf, F., Angerer, P. & Theis, F. SCANPY: large-scale single-cell gene expression data
903 analysis. *Genome Biol* 19, 15 (2018).
- 904 43. Dries R., Chen J., Del Rossi N., et al. Advances in spatial transcriptomic data analysis.
905 *Genome Res.* 2021 Oct;31(10):1706-1718.
- 906 44. Traag, V.A., Waltman, L. & van Eck, N.J. From Louvain to Leiden: guaranteeing well-
907 connected communities. *Sci Rep* 9, 5233 (2019).
- 908 45. Korsunsky, I., Millard, N., Fan, J. et al. Fast, sensitive and accurate integration of single-
909 cell data with Harmony. *Nat Methods* 16, 1289–1296 (2019).

Supplementary Figures



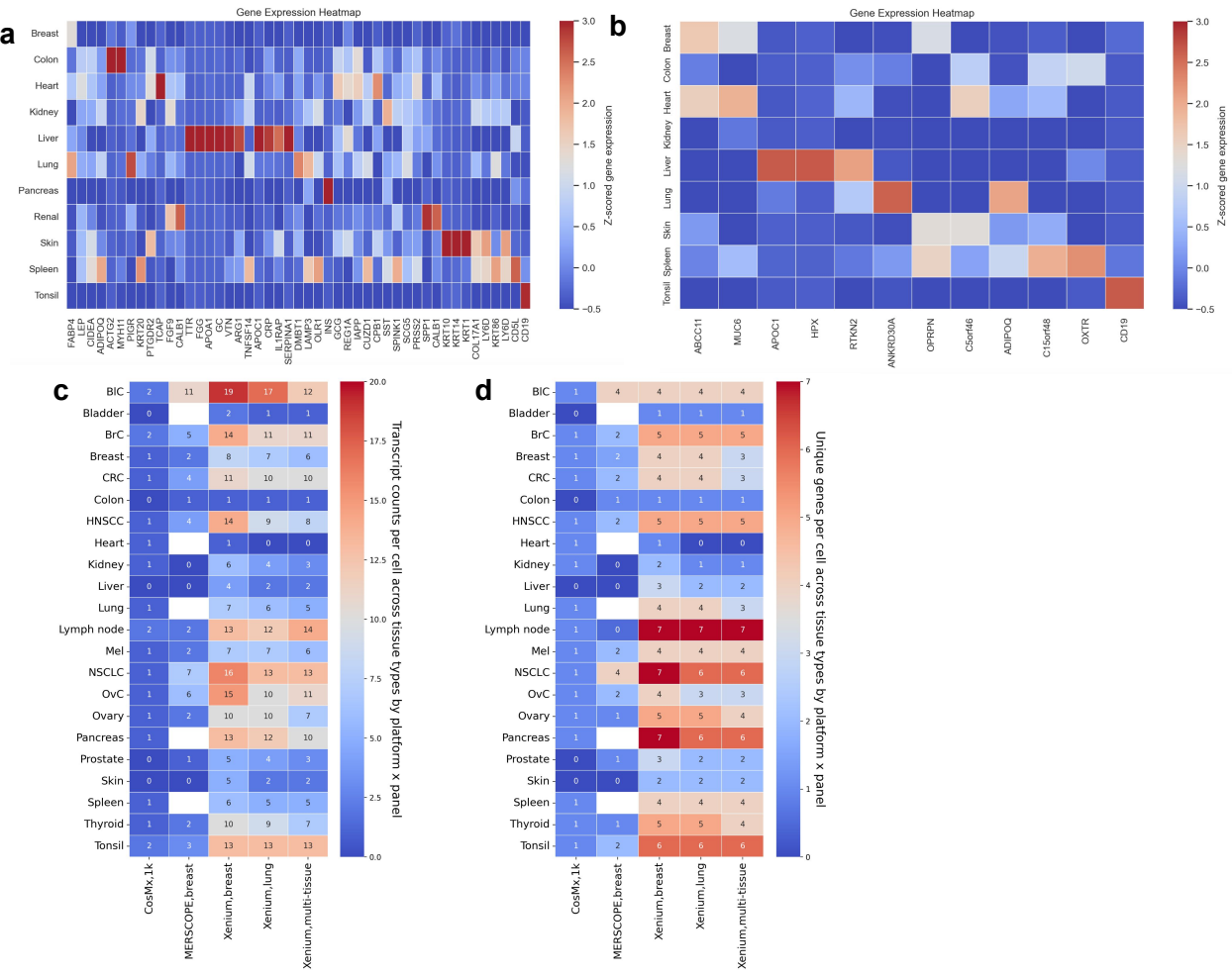
Supplementary Figure 1: Reproducibility across different panels and cores from same patient.

(a) Scatter plots of cumulative gene expression levels (on a logarithmic scale) of shared genes between two panels within each platforms, captured from matched tissue cores. Column 1: Xenium breast vs. Xenium lung; Column 2: Xenium breast vs. Xenium multi-tissue; Column 3: MERSCOPE breast round 1(5 µm) vs. MERSCOPE breast round 2(10 µm). Each data point corresponds to a TMA core. **(b)** Scatter plots of gene expression levels (on a logarithmic scale) of every shared gene between two cores of the same tissue type from the same patient. In this example, cores are from breast cancer tissue. Each data point corresponds to a gene. **(c)** Heatmap of correlation coefficient expressed as Pearson's r values, indicating good core-to-core or sample-to-sample reproducibility. Core pairs are selected from same tissue/tumor type from the same patients.



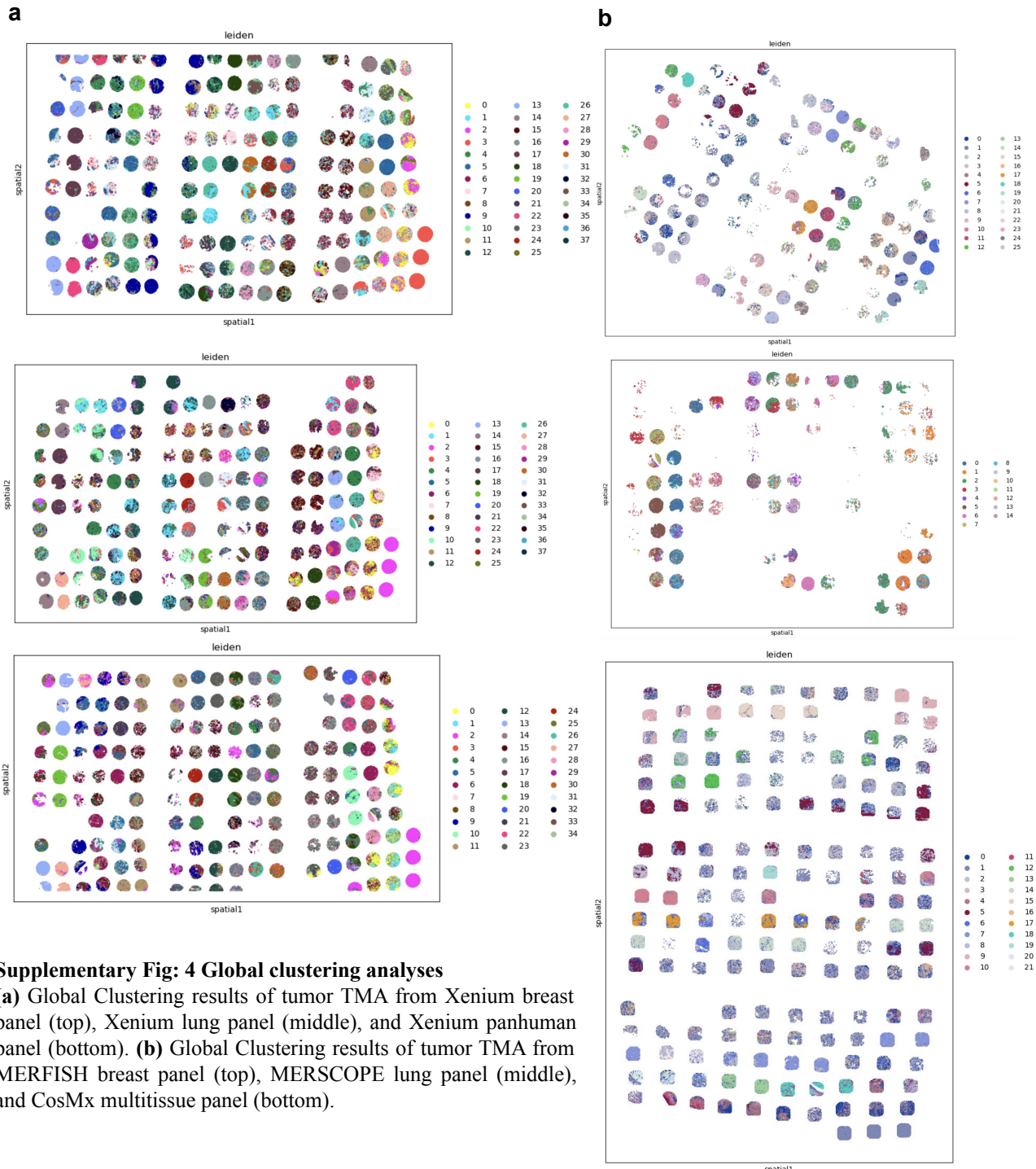
Supplementary Figure 2: Gene by gene plots of iST results by panel and by tissue microarray.

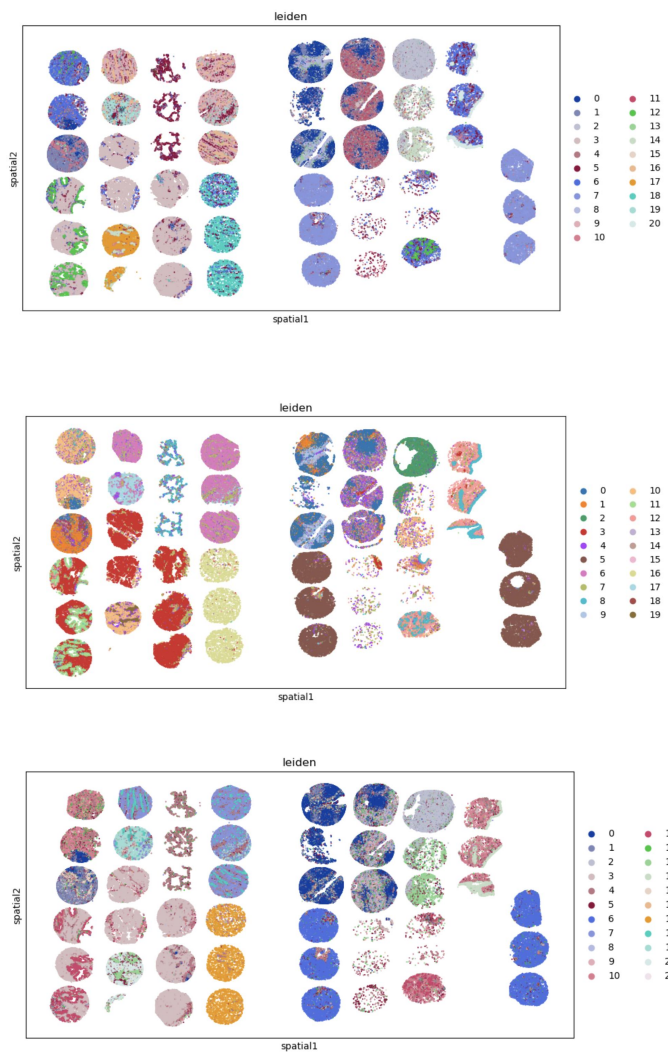
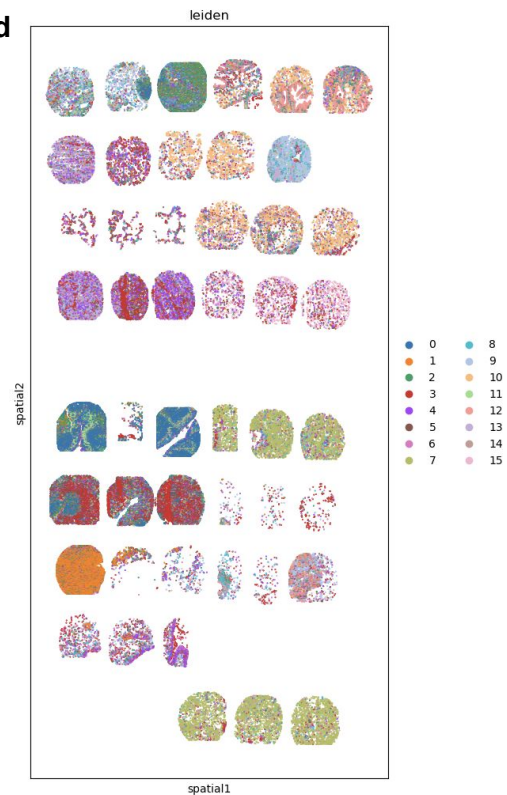
(a) Scatter plots of summed gene expression levels (on a logarithmic scale) of every shared gene between Xenium (breast/lung) and CosMx (1k) data, captured from matched normal tissue TMA cores. Each data point corresponds to a gene. **(b)** Same as (a) but between MERSCOPE (breast/lung) and CosMx(1k). **(c)** Same as (a) but between Xenium(breast/lung) and MERSCOPE(breast/lung). **(d)** Same as (a) but between Xenium(multi-tissue) and CosMx(1k). † denotes the MERSCOPE lung panel acquired with a 5 μm imaging thickness.



Supplementary Figure 3: Tissue marker analyses and cell level measurements.

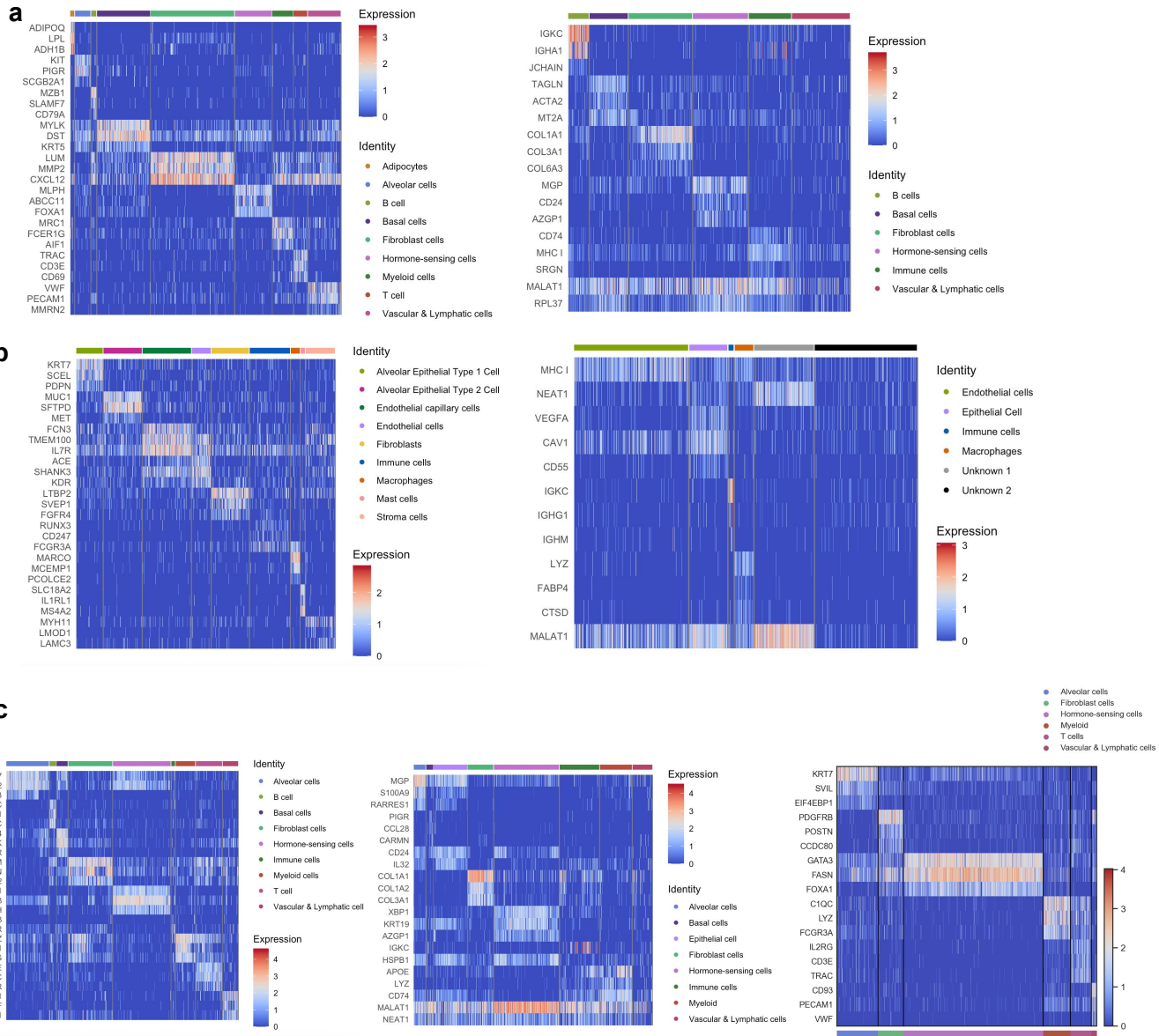
(a) Heatmap of Z-scored gene expression showing CosMx's ability to specifically identify known lineage markers. We focused on the normal tissue TMA profiled with multi-tissue panel and selected genes with canonical expression patterns for this analysis. **(b)** Same as (a) but for MERSCOPE (breast panel). **(c)** Heatmap of transcripts per cell after filtration. Only shared genes (40) are considered here for each panel. **(d)** Same as (c) but showing unique transcripts from the same gene set.



c**d**

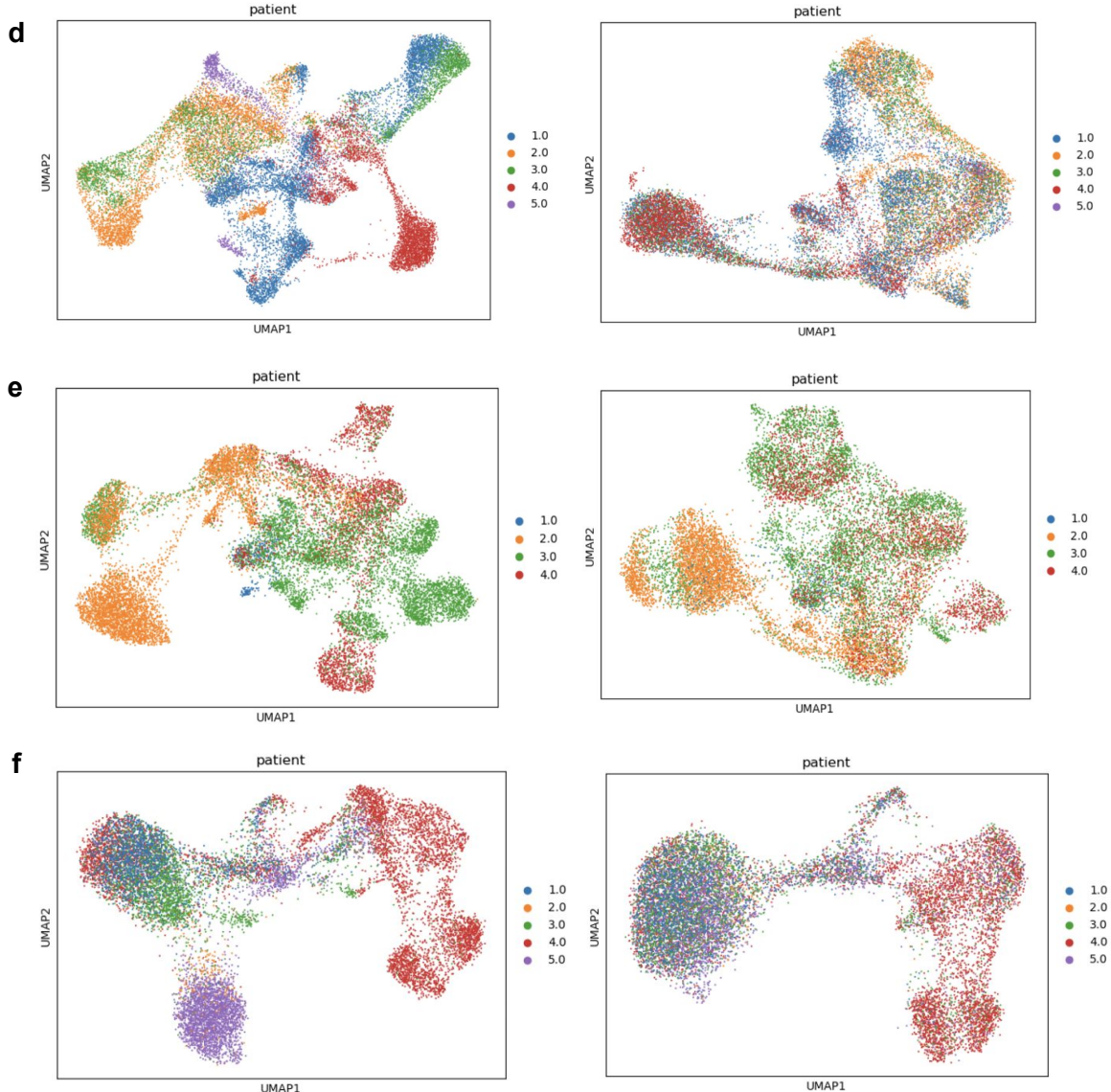
Supplementary Fig: 4 Global clustering analyses

(c) Global Clustering results of normal TMA from Xenium breast panel (top), Xenium lung panel (middle), and Xenium panhuman panel (bottom). (d) Global Clustering results of normal TMA from CosMx multitissue panel (bottom).



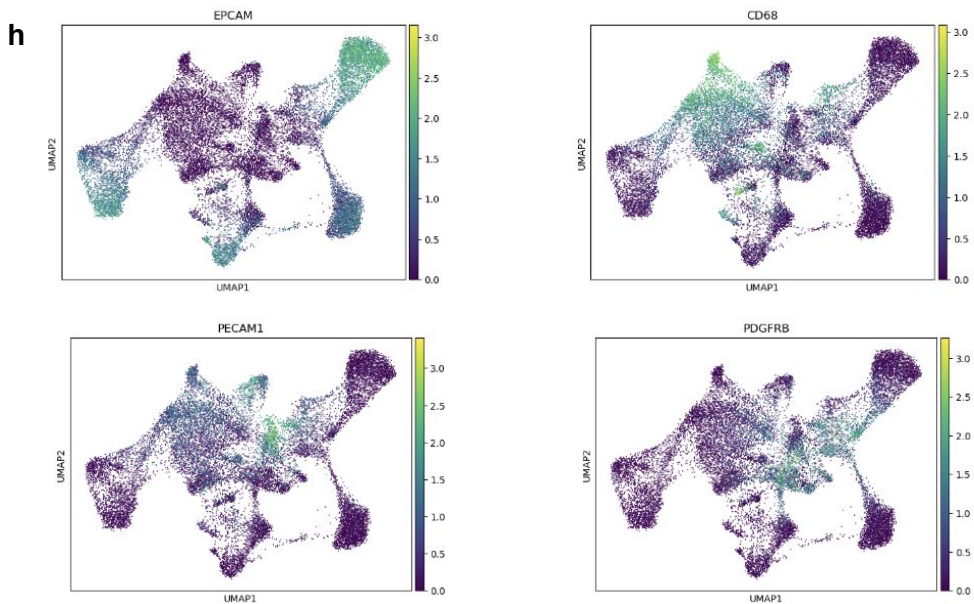
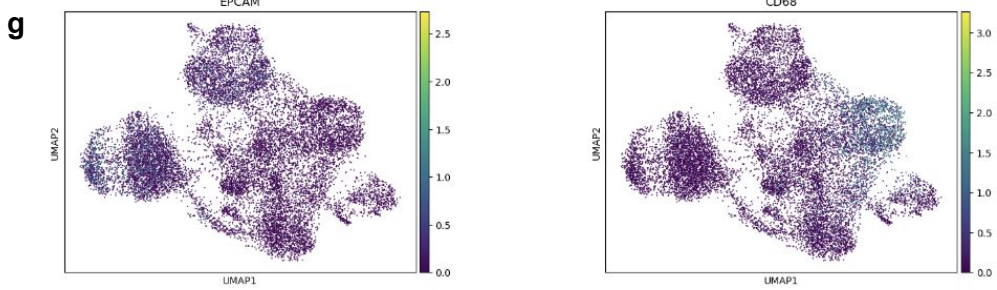
Supplementary Fig: 5. Cell type recovery and UMAPs

(a) Heatmap showing the top gene markers for cell types annotated in breast samples of normal TMA from Xenium breast (left) and Cosmx multitissue (right). **(b)** Heatmap showing the top gene markers for cell types annotated in lung samples of normal TMA from Xenium lung (left) and Cosmx multitissue (right). **(c)** Heatmap showing the top gene markers for cell types annotated in breast cancer samples of tumor TMA from Xenium breast (left), Cosmx multitissue (middle), NERSCOPE breast (right).



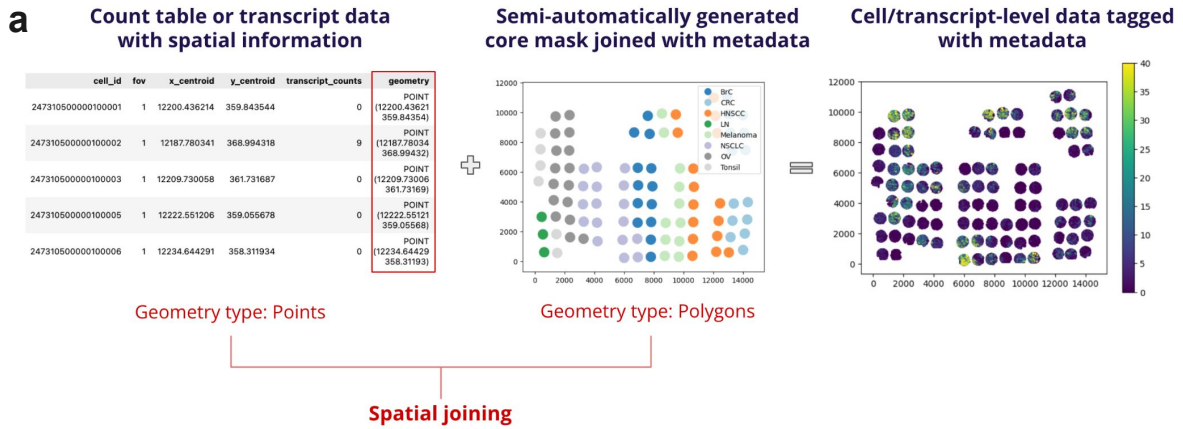
Supplementary Fig: 5. Cell type recovery and UMAPs

(d) UMAP of breast cancer samples of tumor TMA from Xenium breast panel pre (left) and post (right) batch effect removal. (e) UMAP of breast cancer samples of tumor TMA from Cosmx multitissue panel pre (left) and post (right) batch effect removal. (f) UMAP of breast cancer samples of tumor TMA from MERFISH breast panel pre (left) and post (right) batch effect removal



Supplementary Fig: 5. Cell type recovery and UMAPs

(g) UMAP plot of well-known gene markers for BrC, in breast cancer samples of tumor TMA from CosMx multitissue panel. (h) UMAP plot of well-known gene markers for BrC, in breast cancer samples of tumor TMA from Xenium multitissue panel.



Supplementary Figure 6: Workflow for tagging imaging spatial transcriptomics data

(a) To facilitate standardized data formatting and subsequent analytical processes, we built this data ingestion pipeline with the following objectives: 1) to grab cell-level and transcript-level data from diverse platforms and normalize the data structure; 2) to tag each cell and transcript with essential metadata including tissue type, tumor status, PD-L1 status, among others; and 3) to transform the data into various formats tailored to the requirements of particularized analyses. Specifically, to tag the data, core centers in the TMA were pinpointed using DAPI images (Xenium) or cell metadata that contains global coordinates (MERSCOPE and CosMx) using QGIS(version:3.16.10-Hannover). Cells or transcripts within a specified radius were then labeled with core metadata via spatial joining (implemented by GeoPandas, version:0.13.0). In instances where the cores are in close proximity or when a uniform radius cannot be applied effectively, we manually generated the core boundary masks.